



**NAVAL  
POSTGRADUATE  
SCHOOL**

**MONTEREY, CALIFORNIA**

**THESIS**

**VALIDATION OF AN EMPIRICAL MODEL OF HF  
RADIO ABSORPTION DURING SOLAR X-RAY FLARES**

by

Angelica S. Nielsen

March 2022

Thesis Advisor:

Christopher G. Smithtro

Co-Advisor:

Wendell A. Nuss

**Approved for public release. Distribution is unlimited.**

THIS PAGE INTENTIONALLY LEFT BLANK

<b>REPORT DOCUMENTATION PAGE</b>			<i>Form Approved OMB No. 0704-0188</i>
Public reporting burden for this collection of information is estimated to average 1 hour per response, including the time for reviewing instruction, searching existing data sources, gathering and maintaining the data needed, and completing and reviewing the collection of information. Send comments regarding this burden estimate or any other aspect of this collection of information, including suggestions for reducing this burden, to Washington headquarters Services, Directorate for Information Operations and Reports, 1215 Jefferson Davis Highway, Suite 1204, Arlington, VA 22202-4302, and to the Office of Management and Budget, Paperwork Reduction Project (0704-0188) Washington, DC, 20503.			
<b>1. AGENCY USE ONLY (Leave blank)</b>	<b>2. REPORT DATE</b> March 2022	<b>3. REPORT TYPE AND DATES COVERED</b> Master's thesis	
<b>4. TITLE AND SUBTITLE</b> VALIDATION OF AN EMPIRICAL MODEL OF HF RADIO ABSORPTION DURING SOLAR X-RAY FLARES			<b>5. FUNDING NUMBERS</b>
<b>6. AUTHOR(S)</b> Angelica S. Nielsen			
<b>7. PERFORMING ORGANIZATION NAME(S) AND ADDRESS(ES)</b> Naval Postgraduate School Monterey, CA 93943-5000			<b>8. PERFORMING ORGANIZATION REPORT NUMBER</b>
<b>9. SPONSORING / MONITORING AGENCY NAME(S) AND ADDRESS(ES)</b> N/A			<b>10. SPONSORING / MONITORING AGENCY REPORT NUMBER</b>
<b>11. SUPPLEMENTARY NOTES</b> The views expressed in this thesis are those of the author and do not reflect the official policy or position of the Department of Defense or the U.S. Government.			
<b>12a. DISTRIBUTION / AVAILABILITY STATEMENT</b> Approved for public release. Distribution is unlimited.			<b>12b. DISTRIBUTION CODE</b> A
<b>13. ABSTRACT (maximum 200 words)</b>  Military operations depend on high frequency (HF) radio communication. During a solar x-ray flare, the D-region of the ionosphere absorbs the HF radio wave energy, attenuating the signal, causing critical communication lines to fail. This research evaluates the performance of two empirical models that measure solar flare-induced HF absorption: The D-region Absorption Prediction (DRAP) model provided by the Space Weather Prediction Center and the Empirical HIDIVE Absorption (EHA) model developed by Air Force Institute of Technology's Evelyn Schumer in her 2010 dissertation. The DRAP model scales frequency as $f^{-1.5}$ while normalizing the data by a $\cos^{0.75}(\chi)$ dependence. The EHA model is scaled as $f^{-1.24}$ and normalizes by a $\cos^{0.9}(\chi)$ dependence. Our statistical regression model improves flare-induced HF absorption modeling capabilities. It is built to perform at the 30 MHz frequency for the midlatitude riometers and normalizes the data using $\cos^{1.0}(\chi)$ . We found the EHA model has a bias to overpredict flare size while the DRAP model trends to underpredict absorption. Our model outperforms the DRAP and EHA models for predicting solar flare induced HF absorption with the lowest RMSE value at 0.267, while the EHA model performed second best with an RMSE of 0.862 and the DRAP had an RMSE at 1.007.			
<b>14. SUBJECT TERMS</b> signal attenuation, sudden ionospheric disturbance, SID, shortwave fadeout, SWF, predicting solar x-ray flares, midlatitude D-region ionospheric absorption, high frequency, HF, radio signals, ionospheric modeling, HF propagation prediction, HF absorption, space weather, military operations communications, Empirical HIDIVE Absorption, EHA, D-region Absorption Prediction, DRAP			<b>15. NUMBER OF PAGES</b> 79
			<b>16. PRICE CODE</b>
<b>17. SECURITY CLASSIFICATION OF REPORT</b> Unclassified	<b>18. SECURITY CLASSIFICATION OF THIS PAGE</b> Unclassified	<b>19. SECURITY CLASSIFICATION OF ABSTRACT</b> Unclassified	<b>20. LIMITATION OF ABSTRACT</b> UU

THIS PAGE INTENTIONALLY LEFT BLANK

**Approved for public release. Distribution is unlimited.**

**VALIDATION OF AN EMPIRICAL MODEL OF HF RADIO ABSORPTION  
DURING SOLAR X-RAY FLARES**

Angelica S. Nielsen  
Captain, United States Air Force  
AS, Physics, College of the Canyons, 2015  
AS, Mathematics, College of the Canyons, 2015  
BS, California State University - Channel Islands, 2017

Submitted in partial fulfillment of the  
requirements for the degree of

**MASTER OF SCIENCE IN METEOROLOGY**

from the

**NAVAL POSTGRADUATE SCHOOL  
March 2022**

Approved by: Christopher G. Smithtro  
Advisor

Wendell A. Nuss  
Co-Advisor

Wendell A. Nuss  
Chair, Department of Meteorology

THIS PAGE INTENTIONALLY LEFT BLANK

## ABSTRACT

Military operations depend on high frequency (HF) radio communication. During a solar x-ray flare, the D-region of the ionosphere absorbs the HF radio wave energy, attenuating the signal, causing critical communication lines to fail. This research evaluates the performance of two empirical models that measure solar flare-induced HF absorption: The D-region Absorption Prediction (DRAP) model provided by the Space Weather Prediction Center and the Empirical HIDIVE Absorption (EHA) model developed by Air Force Institute of Technology's Evelyn Schumer in her 2010 dissertation. The DRAP model scales frequency as  $f^{-1.5}$  while normalizing the data by a  $\cos^{0.75}(\gamma)$  dependence. The EHA model is scaled as  $f^{-1.24}$  and normalizes by a  $\cos^{0.9}(\gamma)$  dependence. Our statistical regression model improves flare-induced HF absorption modeling capabilities. It is built to perform at the 30 MHz frequency for the midlatitude riometers and normalizes the data using  $\cos^{1.0}(\gamma)$ . We found the EHA model has a bias to overpredict flare size while the DRAP model trends to underpredict absorption. Our model outperforms the DRAP and EHA models for predicting solar flare induced HF absorption with the lowest RMSE value at 0.267, while the EHA model performed second best with an RMSE of 0.862 and the DRAP had an RMSE at 1.007.

THIS PAGE INTENTIONALLY LEFT BLANK

# TABLE OF CONTENTS

<b>I.</b>	<b>INTRODUCTION.....</b>	<b>1</b>
<b>A.</b>	<b>PROBLEM STATEMENT .....</b>	<b>1</b>
<b>B.</b>	<b>RESEARCH QUESTIONS.....</b>	<b>2</b>
<b>C.</b>	<b>METHODOLOGY .....</b>	<b>2</b>
<b>D.</b>	<b>THESIS OVERVIEW .....</b>	<b>2</b>
<b>II.</b>	<b>THEORETICAL BACKGROUND .....</b>	<b>5</b>
<b>A.</b>	<b>IONOSPHERE.....</b>	<b>5</b>
<b>B.</b>	<b>RADIO WAVE PROPAGATION AND ABSORPTION.....</b>	<b>8</b>
<b>D.</b>	<b>RADIO BLACKOUT .....</b>	<b>11</b>
<b>E.</b>	<b>STONEHOCKER’S MODEL DEVELOPMENT .....</b>	<b>12</b>
<b>F.</b>	<b>SPACE WEATHER PREDICTION CENTER .....</b>	<b>13</b>
<b>G.</b>	<b>SCHUMER’S EMPIRICAL HIDIVE D-REGION     ABSORPTION MODEL .....</b>	<b>15</b>
<b>H.</b>	<b>RIOMETERS .....</b>	<b>15</b>
<b>III.</b>	<b>DATA PREPARATION.....</b>	<b>19</b>
<b>A.</b>	<b>FLARE SELECTION.....</b>	<b>19</b>
<b>B.</b>	<b>RIOMETER DATA PREPARATION.....</b>	<b>29</b>
<b>C.</b>	<b>BASELINE OF RIOMETER ABSORPTION TO ZERO .....</b>	<b>30</b>
<b>IV.</b>	<b>MODEL CREATION.....</b>	<b>35</b>
<b>A.</b>	<b>NORMALIZING PREDICTED ABSORPTION TO DEVELOP     A MODEL FRAMEWORK.....</b>	<b>35</b>
<b>B.</b>	<b>COMPARISON OF MODELS.....</b>	<b>38</b>
<b>C.</b>	<b>RMSE COMPARISON .....</b>	<b>42</b>
<b>D.</b>	<b>HALLOWEEN FLARE .....</b>	<b>43</b>
<b>V.</b>	<b>CONCLUSION .....</b>	<b>47</b>
	<b>APPENDIX A. MODEL FLARE LIST .....</b>	<b>51</b>
	<b>APPENDIX B. CONTROL FLARE LIST .....</b>	<b>53</b>
	<b>LIST OF REFERENCES.....</b>	<b>55</b>
	<b>INITIAL DISTRIBUTION LIST .....</b>	<b>61</b>

THIS PAGE INTENTIONALLY LEFT BLANK

## LIST OF FIGURES

Figure 1.	The electron density profile of the ionosphere as a function of altitude. Source: NASA (2013).....	6
Figure 2.	HF radio wave propagation in the ionosphere. Source: Olsen (2005).....	9
Figure 3.	X-ray flux measurements for the 4 November 2003 flare event. Source: Möller (2021).....	11
Figure 4.	Riometer data measured in voltage depicting absorption signatures recorded over a 3-day period. Source: University of Calgary (2005).....	17
Figure 5.	Quiet day curve fit to one day of raw data. Source: University of Calgary (2005). ....	18
Figure 6.	Absorption recorded in decibels by the TALO riometer on 14 July 2000. Adapted from NOAA (2020); University of Calgary (2021). ....	22
Figure 7.	Proton flux measured during the 14 July 2000 event. Source: European Space Agency (2021).....	23
Figure 8.	Absorption recorded at the MCMU riometer from 0900-2400 UT on 15 July 2000 during a large geomagnetic storm. Adapted from NOAA (2020); University of Calgary (2021).....	25
Figure 9.	Kp-index for the 15 July 2000 flare event. Source: Thuesner (2021). ....	26
Figure 10.	Absorption correlating with x-ray flux during the 02 April 2001 flare event for the ESKI riometer station. ....	27
Figure 11.	Kp index for the 02 April 2001 absorption event. Source: Thuesner (2021).....	28
Figure 12.	The baselined absorption measured at ISLL observatory on 7 June 2000. Adapted from NOAA (2020); University of Calgary (2021). ....	31
Figure 13.	The 07 June 2000 flare event recorded by the ISLL riometer station showing absorption as a function of x-ray flux. Adapted from NOAA (2020); University of Calgary (2021).....	32
Figure 14.	The baselined absorption measured at the RANK station on 15 July 2004. Adapted from NOAA (2020); University of Calgary (2021). ....	33

Figure 15.	The 15 July 2004 flare event recorded by the RANK riometer station showing absorption as a function of x-ray flux. Adapted from NOAA (2020); University of Calgary (2021).....	34
Figure 16.	Our model is applied as a fit to the normalized absorption versus x-ray flux data. Adapted from NOAA (2020); University of Calgary (2021).....	36
Figure 17.	Absorption (black line) recorded at the ISLL observatory during a solar flare on 15 July 2004 from the model list. Adapted from NOAA (2020); University of Calgary (2021).....	39
Figure 18.	Comparison of predictive performance for the 13 July 2004 control list flare event at RANK riometer station. Adapted from NOAA (2020); University of Calgary (2021). ....	40
Figure 19.	The 2 April 2001 flare event at the TALO observatory. Adapted from NOAA (2020); University of Calgary (2021).....	41
Figure 20.	The 04 November 2003 flare at FSMI observatory during the Halloween storms. Adapted from NOAA (2020); University of Calgary (2021). ....	44

## LIST OF TABLES

Table 1.	X-ray flare classification. Source: NASA (2021). .....	10
Table 2.	Correlation between radio blackout and solar flare strength. Source: SWPC (2021). .....	12
Table 3.	NORSTAR riometer array. Adapted from Rogers and Honary (2015). .....	16
Table 4.	Model fits for different normalization coefficients, $r$ .....	38
Table 5.	RMSE comparisons between the models. ....	42
Table 6.	Predicted magnitude for the 04 November 2003 flare. ....	45

THIS PAGE INTENTIONALLY LEFT BLANK

## LIST OF ACRONYMS AND ABBREVIATIONS

CNA	Cosmic Noise Absorption
CME	Coronal Mass Ejection
DRAP	D-Region Absorption Prediction
EUV	Extreme Ultraviolet Radiation
GOES	Geostationary Operational Environmental Satellite
HAF	Highest Affected Frequency
HF	High Frequency
HIDIVE	HF Investigation of D-region Ionospheric Variation Experiment
LUF	Lowest Usable Frequency
MUF	Maximum Usable Frequency
NOAA	National Oceanic and Atmospheric Administration
RFI	Radio Frequency Interference
RIOMETER	Relative Ionospheric Opacity Meter
QDC	Quiet Day Curve
SEP	Solar Energetic Particles
SPE	Solar Proton Event
SID	Sudden Ionospheric Disturbance
SWF	Short-Wave Fadeout
SWPC	Space Weather Prediction Center
UT	Universal Time

THIS PAGE INTENTIONALLY LEFT BLANK

## **ACKNOWLEDGMENTS**

To my husband and family, thank you for all of the love and encouragement throughout the years. To Professor Smithtro and Professor Nuss, thank you for your endless patience and support. You helped me find passion through science and geared me toward making a difference where I can. You've both guided my future and forever have my gratitude. Final thanks to the Canadian Space Agency for the open publication of the riometer datasets, which can be accessed through the Open Government Portal (University of Calgary, 2021). This thesis is dedicated in loving memory to my godmother.

THIS PAGE INTENTIONALLY LEFT BLANK

# I. INTRODUCTION

## A. PROBLEM STATEMENT

Space weather events can pose a threat to national security by impacting infrastructure and communication systems. High frequency (HF) radio is a method of long-distance communication used by the military, civil aviation, and disaster response agencies. HF radio waves are electromagnetic waves with frequencies that range from 3 to 30 MHz. Radio waves are susceptible to attenuation and become absorbed during space weather events, preventing the signal from transmitting. Loss of HF radio communication caused mission-critical impacts during disaster relief efforts and were noted as problematic by emergency communications personnel performing aviation tracking (Redmon et al., 2018). The Space Weather Prediction Center (SWPC) provides forecasts of solar activity so government agencies can be better postured to account for future space weather events.

One particular focus of SWPC is forecasting radio blackout storms, which are caused when solar flares emit powerful x-rays that degrade HF radio communication (SWPC, 2021b). SWPC categorizes the loss of radio communication due to space weather events on a “radio blackout scale.” The lower categories of radio blackout can cause minor to occasional loss of communication on the sunlit side of the Earth, while the most extreme categories can cause disruption over most of the sunlit side of the Earth for many hours (SWPC, 2021a). Thus, space weather events can critically impact military operations, humanitarian aid, the economy, and infrastructure (Redmon et al., 2018).

Improving model prediction will allow decision-makers to better mitigate the impact of future solar flare events (White House, 2015). The SWPC (2021c) developed the D-region Absorption Prediction (DRAP) model, which is the primary tool government agencies use to monitor radio blackouts caused by solar flares. The DRAP has been improved in recent years to optimize its predictive capabilities based on the work of Sauer and Wilkinson (2008).

Despite the improvements, the DRAP model currently under-predicts HF induced absorption (Schumer, 2010). To improve upon the DRAP model, Schumer (2010)

developed the Empirical HIDIVE D-region Absorption (EHA) model. Schumer found the EHA model outperformed DRAP for higher signal frequencies, particularly at 15 MHz. The EHA model overestimated the absorption at 30 MHz, demonstrating the need to further improve model prediction capabilities.

## **B. RESEARCH QUESTIONS**

What methods can be used to validate the efficacy of the DRAP and EHA absorption models to verify their predictive performance? How can a new model framework optimize the DRAP and EHA models? How has this new framework improved flare induced HF absorption prediction modeling?

## **C. METHODOLOGY**

Our model improves upon Schumer's work. We focus on the 30 MHz frequency, using 13 riometer stations located throughout Canada known as the NORSTAR riometer array. We limited our analysis to absorption caused by solar flare events to ensure the best overall fit for our statistical regression model. Our model parameters were calculated using a test group (the model flare list) and made root mean square error (RMSE) calculation comparisons using a control group (the control flare list) with an appropriate sample size to confirm the predictive performance of each model.

We compared our model to the performance of the DRAP and EHA and found it outperforms both for absorption at 30 MHz for the NORSTAR midlatitude riometer array. Our model is then applied to predict the x-ray flux for the well-known Halloween 2003 flare event, which was so extreme the solar x-ray flux saturated the Geostationary Operational Environmental Satellite (GOES) sensors. Our prediction is in line with the flare magnitude suggested by other researchers, further validating our results.

## **D. THESIS OVERVIEW**

Chapter II provides the theoretical background needed to understand how HF communication is impacted by solar flare events. Chapter III explains how the data was prepared to optimize our model's fit. Chapter IV describes the creation of our model. Chapter V, then, analyzes the DRAP, EHA, and our model to compare the performance of

each for predicting flare-induced HF absorption. We validate each and confirm that our model performs better than the DRAP and EHA over the control group. Lastly, Chapter VI presents the conclusions and recommendations for future research.

THIS PAGE INTENTIONALLY LEFT BLANK

## II. THEORETICAL BACKGROUND

HF communication relies on propagation through the atmosphere to transmit a signal. Solar flares cause a phenomenon known as radio blackout, which is when radio waves are absorbed within the ionosphere. Increased absorption can lead to a failure of HF radio links, which motivates us to develop methods to predict such events to mitigate the operational impacts. The original model created by Stonehocker (1970) laid the groundwork for forecasting flare-induced absorption. Stonehocker's work pre-dates the ability to measure the x-ray flux associated with a solar flare, so he focused on a method based on optical flare importance and applied it to 5 MHz frequency signals. Stonehocker then scaled the 5 MHz attenuation results to predict the absorption at other frequencies. The SWPC used Stonehocker's scaling relationship to develop the DRAP but used x-ray flare classification instead of flare importance. The EHA model also adjusts the frequency and normalization scaling factors, but was developed to perform well at higher frequencies, where the DRAP tends to fall short.

A riometer can record the activity associated with absorption. Since x-ray flux can be correlated with absorption, a riometer can be used to interpret if a solar flare event is occurring. If the absorption is attributed to a solar flare event within the ionosphere, then the DRAP, EHA, and our model can make real-time predictions to mitigate the communication impacts associated with HF induced absorption.

### A. IONOSPHERE

The Earth's atmosphere contains several different layers. Each layer has unique chemistry and temperature profiles which play a crucial role in their formation. The ionosphere is the region in the atmosphere where charged particles (plasma) play an important role; this region undergoes substantial changes in composition during space weather events. This is due to the formation of the ionosphere hinging on the Sun as a source of ionizing radiation. The sun contributes high energy ionization sources such as alpha particles, beta particles, gamma rays, and x-rays (SWPC, 2019). These sources alter the plasma density of the ionosphere, where HF radio waves refract.

Figure 1 illustrates how the plasma density varies with altitude forming different regions within the ionosphere known as the D, E, F1, and F2 regions. In Figure 1, a red line depicts a notional value for the electron density as a function of height. The electron density also varies diurnally, seasonally, with solar activity, and as a function of location on the Earth (Olsen, 2009). The ionosphere extends from roughly 50 km up to more than 1000 km. The D-region electron density increases to roughly  $10^4$  electrons/cm<sup>3</sup> at 90 km. The electron density continues to increase with altitude; at noon the E-region electron density peaks at  $2 \times 10^5$  el/cm<sup>3</sup> near 110 km. The F1-region has a max electron density of  $3 \times 10^5$  el/cm<sup>3</sup>; the maximum occurs near noon and the F1-region disappears at night. The F2 peak occurs near 300 km and is an order of magnitude higher than the F1 peak density reaching values of roughly  $2.5 \times 10^6$  el/cm<sup>3</sup> in winter and  $7 \times 10^5$  el/cm<sup>3</sup> in the summer.

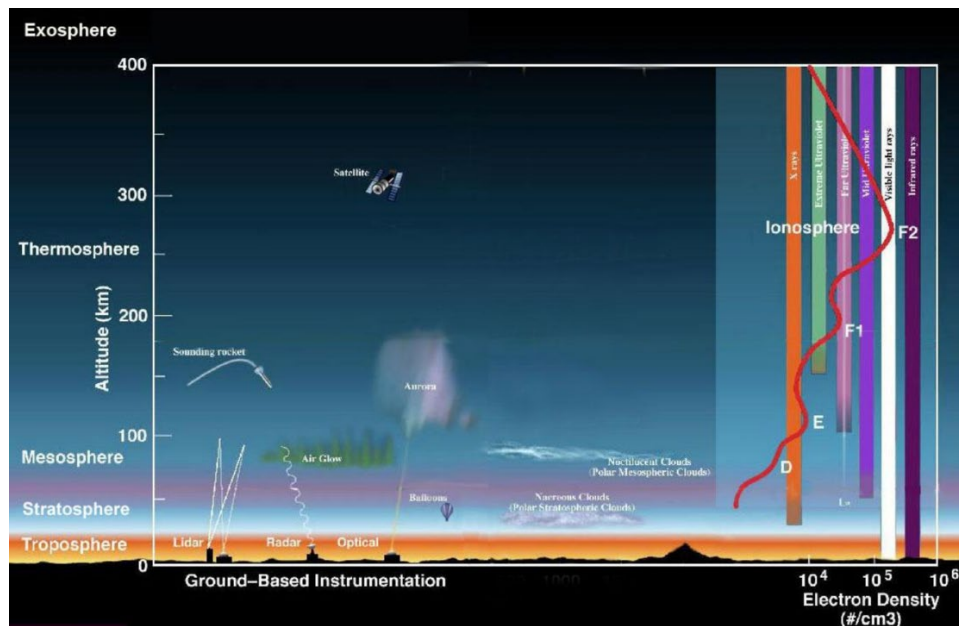


Figure 1. The electron density profile of the ionosphere as a function of altitude. Source: NASA (2013).

The F-region of the ionosphere starts at 140 km and extends beyond 400 km. The F-region is divided into the F1 and F2 layers. The “topside” ionosphere lies above the F2 peak electron concentration. The F2-region is the uppermost layer of the F-region located at a range of 200 km to 400 km (Olsen, 2009). Extreme ultraviolet (EUV) radiation from

the sun ionizes neutral gases to create plasma. Photons with wavelengths in the range of 20-90 nm ionize molecular gases ( $N_2$ ,  $O_2$ ) and atomic oxygen (O), forming  $O_2^+$ ,  $N_2^+$ , and  $NO^+$ .

The F1-region appears as a ledge in the electron density profile located at 140 km and 200 km. It undergoes the same photoionization reactions as the F2-region but has a much higher concentration of neutral densities because it is lower in the atmosphere. Plasma diffusion transports the free electrons from the photoionization reactions in the F1 to the F2-region, causing the peak electron density to occur within the F2-region at 300 km (Olsen, 2009).

The E-region of the ionosphere ranges from 90 and 140 km and differs from the F-region as the primary ionization source is Lyman- $\beta$  hydrogen radiation, which is a high-energy ultraviolet emission that ionizes oxygen  $O_2$ . X-ray ionization of  $N_2$  and  $O_2$  is a secondary process where the  $N_2^+$  ions chemically react and give rise to the dominant ion species  $O_2^+$  and  $NO^+$  (Olsen, 2009).

The D-region is located at the lowest level of the ionosphere and ranges from 60 km to 90 km (Olsen, 2009). The high neutral density found in the D-region is key to its formation. The Lyman- $\alpha$  line of solar radiation causes the formation of the D-region by ionizing nitric oxide (NO). Solar x-rays also ionize  $N_2$  and  $O_2$  as a secondary ionization mechanism. X-ray ionization occurs in a minimal amount except during solar flares. When solar flares occur, the resulting increase in ionization hinders the transmission of HF radio wave communication. At night, the lack of solar radiation allows electrons to recombine, resulting in the D-region disappearing for most locations except at latitudes exceeding  $65^\circ$ . This is because energetic particles contribute as an ionizing radiation source that sustains the formation of the D-region. Thus, nighttime locations do not experience the same impact from a solar flare as the sunlit regions.

The key takeaway is the ionosphere differs from the neutral atmosphere because of the variation of the electron density caused by different ionization sources for each region. When the sun emits additional radiation, the composition of the ionosphere changes.

Increases to the ionosphere's electron density affect the transmission of HF radio wave communication because the signal cannot propagate through the medium.

## B. RADIO WAVE PROPAGATION AND ABSORPTION

HF (3-30 MHz) radio wave propagation can be explained through Snell's law, which outlines how a change of the refractive index alters the path of electromagnetic radiation. HF radio waves propagate upward in primarily a straight path through Earth's lower atmosphere. Once the wave reaches about 50 km, it enters the ionosphere and begins to suffer both absorption and refraction. HF radio waves typically continue propagating until they completely reflect, often in the F2-region of the ionosphere due to the greater electron densities found there. Depending on the frequency of the signal and on the state of the ionosphere, it is also possible the HF radio waves will not reflect and simply pass through the ionosphere.

Radio wave propagation is summarized by the Appleton formula (Davies, 1965) in which  $n$  defines the index of refraction in a plasma and is approximated by

$$n = \sqrt{1 - \frac{f_p^2}{f^2}}, \quad (1)$$

where  $f$  is the incident radio frequency and  $f_p$  is the plasma frequency, both in kHz. The plasma frequency is given by  $f_p \cong 9\sqrt{N_e}$  ( $\text{cm}^3$ ), and depends on the square root of the electron density  $N_e$ . The index of refraction in a plasma  $n$  is then applied using Snell's law

$$n_o \sin \theta_o = n_1 \sin \theta_1, \quad (2)$$

which describes the change of a signal's propagation angle across an interface in terms of the indices of refraction. Here,  $n_o$  is the index of refraction and  $\theta_o$  is the angle on one side of the interface, while  $n_1$  and  $\theta_1$  are the index and angle on the other side. When a radio wave signal enters the atmosphere, we can imagine it starting with an initial angle  $\theta_o$ . The signal continues to travel upward until it reaches the ionosphere, at which point the electron density begins to increase and the ray refracts. Figure 2 shows reflection occurs when  $\theta =$

90°; the wave then travels back to Earth, where  $n = 1$  and returns with the same angle it began with,  $\theta_0$ .

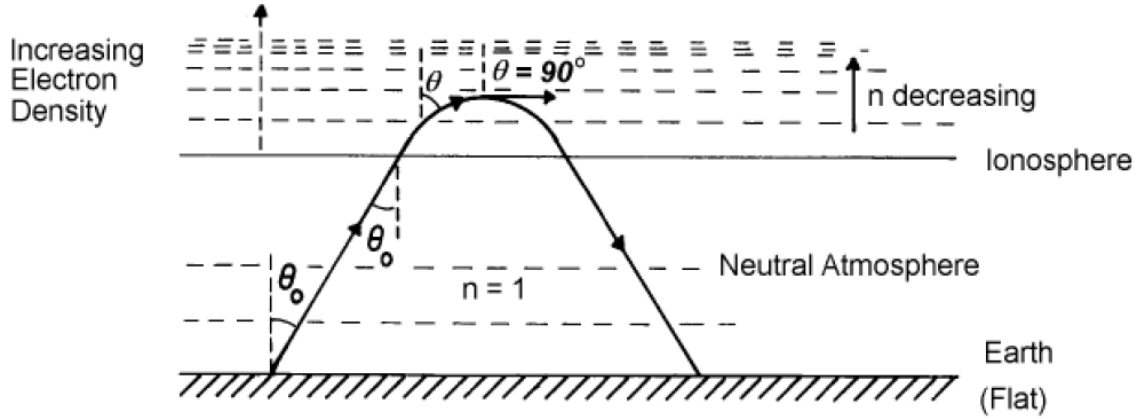


Figure 2. HF radio wave propagation in the ionosphere. Source: Olsen (2005).

The lower regions of the ionosphere maintain lower plasma densities than the F-region allowing HF radio waves to propagate to the F-region, where the signal undergoes more refraction due to the higher plasma density. In HF sky-wave propagation, the signal refracts completely, causing signals to return to Earth. However, the location of reflection depends on the frequency of the transmitted signal.

The D-region is unique from the other layers since the chemistry causes free electrons to take energy from the propagating signal resulting in absorption. This appears as attenuation in the received signal. The signal absorption is inversely proportional to the square of the transmitted frequency and is given by

$$K \propto \frac{N\nu}{f^2}, \quad (3)$$

where  $K$  is the absorption coefficient,  $f$  is the signal frequency,  $N$  is electron density, and  $\nu$  is the electron-neutral collision frequency.

Solar flares increase the flux of soft x-rays and EUV photons, which increases the ionization rate, enhancing the electron density in the D-region (Yasyukevich et al., 2018).

As a result, HF communication signals can become absorbed in the D-region during a solar flare. According to Equation (3), this absorption is minimized for higher signal frequencies; as an example, the absorption would be lower at 30 MHz than 15 MHz.

### C. SOLAR FLARES

Solar flares are explosive releases of stored magnetic energy in the Sun’s atmosphere. Convective motions in the Sun cause local magnetic fields to become twisted and concentrated, which stores magnetic energy (NASA, 2015). When these twisted magnetic field lines reach a critical threshold, the energy can be released explosively, through a process called magnetic reconnection (National Center for Atmospheric Research, 2021). The event can last for only a few minutes or persist for several hours.

Solar flare intensity can be classified based on the strength of the x-ray flux, as seen in Table 1. Solar flares are classified based on the peak intensity of the x-ray flux, where each category represents a 10-fold increase in power. An X class flare is 10 times more powerful than an M class flare. An M class flare is 10 times more powerful than a C class. Thus, A, B, and C class flares are weaker with lower peak x-ray flux emission. M and X class flares impart significantly higher peak values of x-ray flux. Flare classification can be broken down even further. For example, based on the scale from Table 1, an M1 class flare equates to a peak flux of  $1 \times 10^{-5} \text{ W/m}^2$ . An M5 class flare corresponds to a peak flux of  $5 \times 10^{-5} \text{ W/m}^2$ . An extreme solar flare event, such as an X20, corresponds to a peak flux  $2 \times 10^{-3} \text{ W/m}^2$ .

Table 1. X-ray flare classification. Source: NASA (2021).

<b>Classification</b>	<b>Flux (W/ m<sup>2</sup>)</b>
X	$>10^{-4}$
M	$10^{-5}$ to $10^{-4}$
C	$10^{-6}$ to $10^{-5}$
B	$10^{-7}$ to $10^{-6}$
A	$<10^{-7}$

Figure 3 provides an example of an X class flare. The size of the flare is one of the largest ever recorded by GOES at X17 ( $1.7 \times 10^{-3} \text{ W/m}^2$ ), which was the maximum measurable value before the detectors were saturated, indicating the flare could have been even larger than recorded.

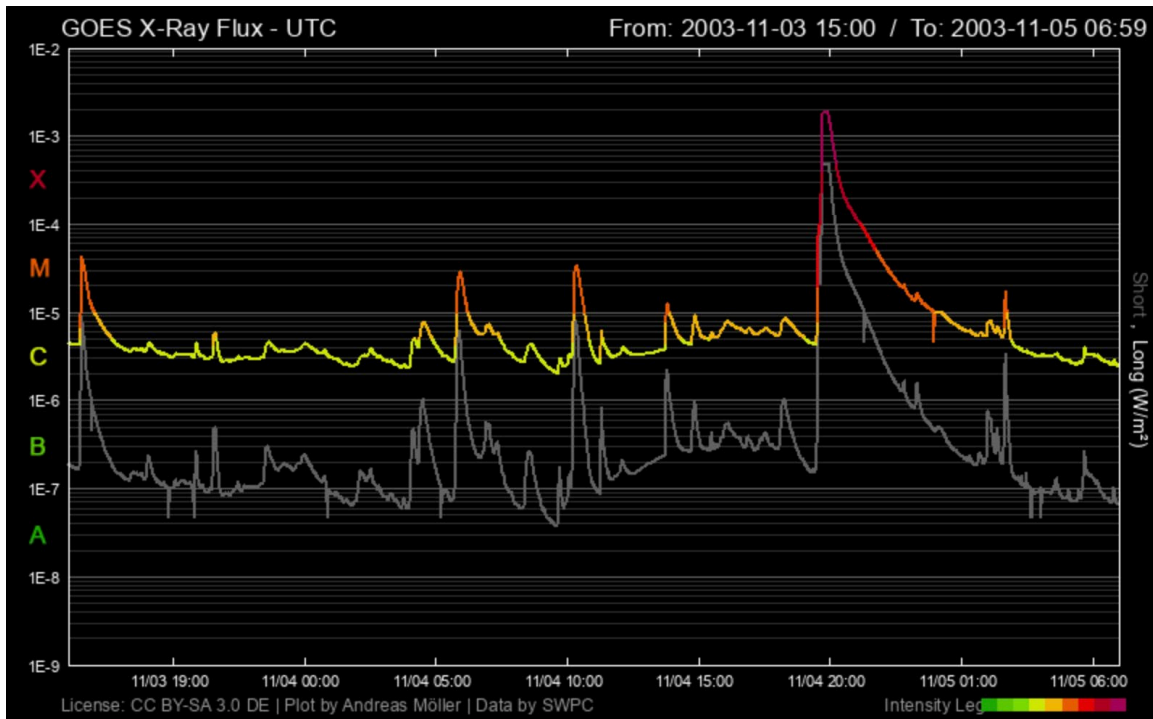


Figure 3. X-ray flux measurements for the 4 November 2003 flare event. Source: Möller (2021). The figure shows both hard (grey line) and soft (colored line) x-rays over time. C-class flares are colored in yellow, M-class in orange, and X class as red. The X class flare has a maximum flux with a magnitude of  $1.7 \times 10^{-3} \text{ W/m}^2$  near 2000 UT on 4 November 2003. The x-ray flux remains elevated until roughly 0600 UT on 5 November.

#### D. RADIO BLACKOUT

During solar flares, the increase in photon flux and the resulting increase in the electron density in the ionosphere inhibit radio wave propagation. Solar x-ray flares are the primary cause of radio blackout in the midlatitudes (Contreira et al., 2005; Yasyukevich, 2018). Radio blackout is a phenomenon where HF radio waves propagating through the ionosphere during a flare become absorbed and are converted to heat within the D-region

due to an increase in electron density, typically caused by a solar flare (Warrington et al., 2012; Warrington et al., 2016). Specifically, additional electrons within the D-region increase the electron collision frequency, which increases the transfer of radio energy to the neutral gases, absorbing the signal. Table 2 classifies radio blackouts by severity. The stronger the flare, the more severe the radio blackout impacts will be on the sunlit side of the Earth.

Table 2. Correlation between radio blackout and solar flare strength.  
Source: SWPC (2021).

Category	X-ray Flare	Flux (W/m <sup>2</sup> )	Severity Descriptor
R1	M1	$1 \times 10^{-5}$	Minor
R2	M5	$5 \times 10^{-4}$	Moderate
R3	X1	$1 \times 10^{-4}$	Strong
R4	X10	$1 \times 10^{-3}$	Severe
R5	X20	$2 \times 10^{-3}$	Extreme

R5 is the most extreme on the radio blackout scale and corresponds to an X20 or greater solar flare. The impacts can occur over many hours for most of the Earth’s sunlit side, inhibiting maritime and aviation systems (SWPC, 2021a; SWPC, 2021b).

## E. STONEHOCKER’S MODEL DEVELOPMENT

Radio blackout was studied extensively by Stonehocker (1970), who developed a model to predict HF signal attenuation based on real-time solar radio burst energy, which was used as a proxy for solar x-ray emission. Stonehocker based his model on the historical probabilities of radio blackout occurrence and the correlation between solar radio flux and signal attenuation established by Harvey (1965). Stonehocker’s model focused on using a classification of flare importance to predict flare-induced absorption for a 5 MHz signal at the subsolar point (the point where the Sun is directly overhead). To account for the

frequency ( $f$ ) dependence of attenuation, he introduced a scale factor of  $f^{-2}$ . This factor relates back to Equation (3), which indicates signal absorption is inversely proportional to the square of the transmitted frequency. Stonehocker (1970) accounted for locations other than the subsolar point using a factor for  $\cos(\chi)$ , where  $\chi$  is the solar zenith angle. The cosine function was applied to estimate attenuation at the one-hop path midpoint or at each control location for multi-hop paths. Stonehocker (1970) found the factor produced errors less than 9% for attenuation predictions at other frequencies when applied to signals between 5 and 12 MHz, confirming that the scaling factor could be applied to model absorption at other frequencies.

Later work explored varying the frequency scaling factor,  $f^k$ , to improve predictions at other frequencies, and introduced an exponent to the scale factor for solar zenith angle,  $\cos^r(\chi)$ . In this work we also used scaling laws for the cosine function,  $\cos^r(\chi)$ , to fit the data. While Stonehocker relied on radio bursts to parameterize the absorption, we use x-ray flux.

## F. SPACE WEATHER PREDICTION CENTER

The D-region Absorption Prediction (DRAP) model predicts HF signal absorption in real-time. It is an empirical model that uses solar zenith angle and signal frequency to calculate absorption during a flare. The SWPC developed the DRAP model to mitigate the operational impacts for HF radio communication caused by both solar x-ray flux and solar energetic proton (SEP) events (SWPC, 2010; SWPC, 2021c). The DRAP initially scaled absorption using the same  $f^{-2}$  relationship as Stonehocker (1970) and Equation (3), which assumes the absorption is inversely proportional to the square of the signal frequency. In recent years, the frequency scaling factor has been updated to  $f^{-1.5}$  based on the work of Sauer and Wilkinson (2008), who focused on radio blackout impacts due to SEP and improved the DRAP framework.

The DRAP model differs from Stonehocker's work since it uses the measured x-ray flux instead of flare importance and solar radio flux (SWPC, 2010). According to Mihail Codrescu (email to author, May 11, 2021), the DRAP model calculates absorption based on solar zenith angle, x-ray flux, and radio wave frequency. The model starts by

calculating the Highest Affected Frequency (HAF). The HAF represents the frequency that suffers 1 dB of attenuation at a zenith angle of  $\chi = 0^\circ$  (i.e., the subsolar point). The HAF is given by

$$f_0 = 10 \cdot \log \left[ flux \left( W \cdot m^{-2} \right) \right] + 65 \text{ MHz} , \quad (4)$$

where  $f_0$  represents the HAF in MHz at the subsolar point and  $flux$  represents the GOES x-ray flux in  $W \cdot m^{-2}$ .

Plasma production, and therefore absorption, decrease moving away from the subsolar point. To account for this effect, the HAF calculated in Equation (4) is scaled by  $\cos^r(\chi)$ , where  $r$  is a fitting parameter and  $\chi$  is the solar zenith angle. The DRAP model assumes a  $\cos^{0.75}(\chi)$  dependence (Akmaev, 2010), so the attenuation at other locations can be predicted by

$$f_n = f_0 \cdot \cos^{0.75}(\chi) , \quad (5)$$

where  $f_n$  represents the new scaled HAF (SWPC, 2010). Finally, the absorption for a specific frequency  $Y(f)$  is given by

$$Y(f) = \left( \frac{f_n}{f} \right)^{1.5} \text{ dB} , \quad (6)$$

where  $f$  is the frequency of interest. In this research, the frequency  $f$  is determined by the available data, which is 30 MHz.

We directly compare the DRAP predictions with our model to evaluate its performance. Akmaev (2010) suggested that further research is needed to improve the validation of the x-ray component of the DRAP model by using well-isolated x-ray flare event data from midlatitude stations. Our research study is informed by Akmaev's recommendation, and we carefully selected flares to avoid solar proton events (SPE) and geomagnetic storm events from contaminating the data set.

## G. SCHUMER’S EMPIRICAL HIDIVE D-REGION ABSORPTION MODEL

The work in this thesis builds on Schumer’s research (2010) and aims to validate the Empirical HIDIVE D-region Absorption (EHA) model. Schumer used x-ray flux data obtained from GOES, HF signal strength data obtained from the HIDIVE experiment (Eccles et al., 2005), and HF propagation data from the NORSTAR riometer in Pinawa, Canada to create the EHA model. Schumer found that flare-induced absorption was best fit using an  $f^{-1.24}$  dependence on signal frequency. Her data demonstrated that during quiet solar periods, diurnal absorption of HF transmissions has a  $\cos^{0.9}(\chi)$  dependence on solar zenith angle, rather than the  $\cos^{0.75}(\chi)$  dependence used by the DRAP. Schumer’s work evaluated the DRAP model when frequency was scaled as  $f^{-2}$ , before SWPC’s later update to an  $f^{-1.5}$  dependence. Schumer (2010) noted the “SWPC model performs well for a 5 MHz signal but begins to under-predict absorption as the signal frequency increases, notably at 30 MHz.” In the EHA model, the absorption,  $Y(U_{Xray}, f, \chi)$ , is given by

$$Y(U_{Xray}, f, \chi) = 2.4E4 \cdot f^{-1.24} \sqrt{U_{Xray}} \cdot \cos^{0.9}(\chi), \quad (7)$$

where  $f$  is the signal frequency,  $\chi$  is the solar zenith angle, and  $U_{Xray}$  is x-ray flux measured by the GOES satellite. Schumer concluded by noting the DRAP model performance degrades with increasing signal frequency.

This thesis aims to evaluate the performance of Schumer and SWPC’s performance at the 30 MHz frequency as well as the scaling of absorption by  $\cos(\chi)$ , which will be referred to as normalization.

## H. RIOMETERS

Riometers measure the intensity of cosmic radio noise, typically between 20 and 70 MHz, to monitor the ionosphere. A riometer measures the variation of radio noise on a zenithal beam over the sidereal day, which means the riometer field of view sweeps through the sky with Earth’s rotation. This creates a regular, periodic curve that acts as a baseline known as a quiet day curve (QDC). The QDC represents the average daily variation of cosmic noise when no significant absorption events occur (Marshall & Cully, 2020; Ogunmodimu et al., 2018; Rogers et al., 2015a; Rogers et al., 2015b).

The University of Calgary’s NORSTAR program encompasses 13 midlatitude riometer stations located throughout Canada. The 13 riometers collect ionospheric absorption data and operate at a frequency of 30 MHz. The University of Calgary provides the information collected by the riometers as an open dataset which was utilized by this research. Table 3 shows the riometers that make up the NORSTAR array. Each location includes the station’s latitude and longitude and a four-digit identifier code. The stations in the table are organized from high to low magnetic latitude. The riometer stations listed in Table 3 were used in this research to measure absorption caused by solar flare activity and validate our model’s performance.

Table 3. NORSTAR riometer array. Adapted from Rogers and Honary (2015).

<b>Riometer</b>	<b>Code</b>	<b>Geodetic lat. (°N)</b>	<b>Geodetic long. (°E)</b>	<b>Magnetic latitude at 50 km altitude (°N)</b>
Taloyoak	TALO	69.54	69.54	79.5
Contwoyto Lake	CONT	65.75	-111.26	73.2
Rankin Inlet	RANK	62.82	-92.11	72.8
Eskimo Point	ESKI	61.11	-94.05	71.1
Fort Churchill	CHUR	58.76	-94.08	68.9
Fort Smith	FSMI	60.03	-111.95	67.6
Fort Simpson	FSIM	61.76	-121.23	67.5
Rabbit Lake	RABB	58.23	-103.68	67.3
Gillam	GILL	56.38	-94.64	66.6
Dawson	DAWS	64.05	-139.11	66.0
Island Lake	ISLL	53.86	-94.66	64.2
Fort McMurray	MCMU	56.65	-111.21	64.5
Pinawa	PINA	50.20	-96.04	60.5

Riometer data provides a method to analyze ionospheric absorption (Ogunmodimu et al., 2018; Rogers et al., 2016). Riometers are radio receivers that detect cosmic radio noise passing through the ionosphere at specific frequencies. When a solar flare or high-energy particle precipitation event occurs, enhanced electron density in the D-region ionosphere attenuates the cosmic radio noise signal; this is known as cosmic noise absorption (CNA).

Figure 4 illustrates a signal recorded by a riometer, from which we can infer CNA signatures. The regular sinusoidal variation of voltage corresponds to the changing background cosmic noise as the Earth rotates. Two absorption events are highlighted in red where the riometer voltage deviates from the QDC and fluctuates rapidly over time; one event occurs late into day one and the other at the end of day two. These absorption features decrease the received signal, resulting in lower voltage measurements.

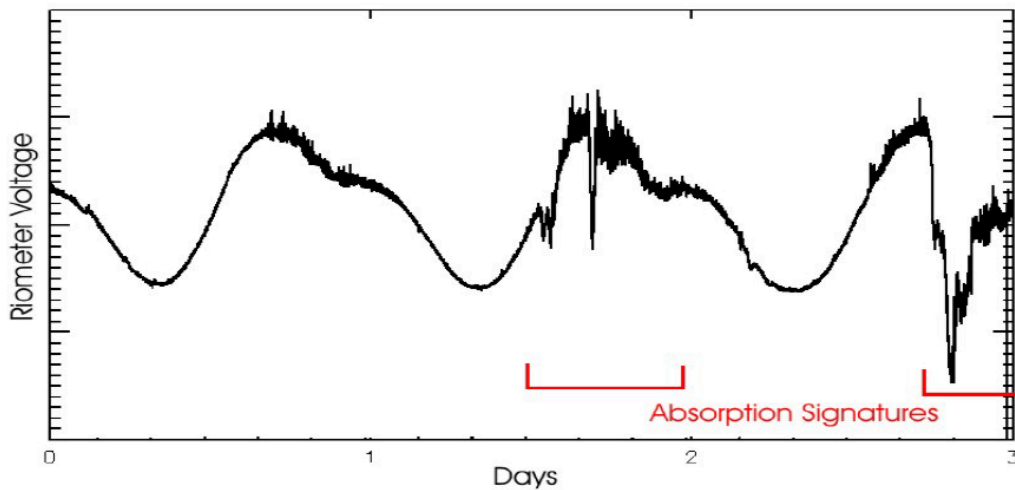


Figure 4. Riometer data measured in voltage depicting absorption signatures recorded over a 3-day period. Source: University of Calgary (2005).

As seen in Figure 4, the background noise signal varies sinusoidally over the course of a day. To determine the CNA, the measured signal is compared to a QDC baseline. Figure 5 illustrates a QDC recorded over a three-day period and fit to the raw riometer data. The QDC is sinusoidal, mirroring the average daily variation when no significant absorption events occur. The cosmic noise absorption is calculated by subtracting the QDC from the recorded signal voltage. As an example, note in Figure 5 that the voltage drops below the QDC at roughly 1300 UT and recovers by the end of the day at 2400 UT; the maximum absorption occurs at roughly 1830 UT. This period represents additional, enhanced absorption in the ionosphere.

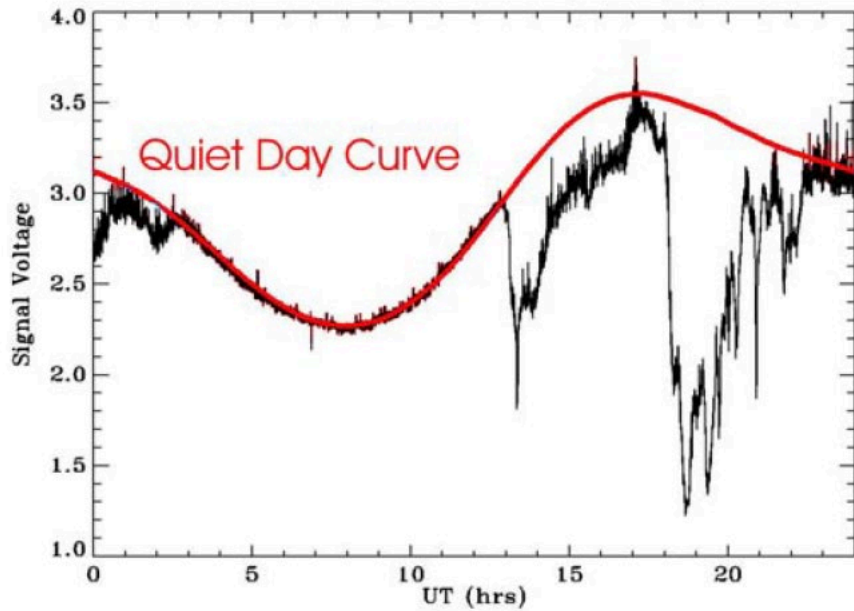


Figure 5. Quiet day curve fit to one day of raw data. Source: University of Calgary (2005).

Riometers do not directly measure the amount of absorption in the ionosphere. Absorption is calculated by subtracting the QDC from the raw riometer data. Differences are attributed to some cause of additional ionization occurring within the ionosphere, such as due to a solar flare, a proton event, or geomagnetic activity (Hargreaves, 1969; Hultqvist, 1966; Longden et al., 2008; Rogers et al., 2015a; Rogers et al., 2015b). These sources of absorption are discussed further in the next chapter.

### III. DATA PREPARATION

To validate the DRAP, EHA, and our model, we carefully select flare-event candidates. This is first done based on flare classification so our model can better fit and predict larger flare events, which is the main goal. We avoid smaller flares since they are typically not strong enough to be observed by the NORSTAR riometers. Next, we screened out potential sources of contamination, such as solar proton events (SPE) and geomagnetic storms, to focus solely on absorption due to x-ray flares.

#### A. FLARE SELECTION

To create our solar flare absorption model, we identified candidate flares for analysis. Flare events were selected based on their class, timing, and season to maximize the chance of observing their effects with the available riometers. Ideally, these flare events should be isolated without other sources of contamination, such as proton events or geomagnetic storms, which would complicate the analysis. To select events for the model flare list, it was important to attribute the source of absorption recorded by the riometers. We looked for indicators of geomagnetic storms and solar protons during the same periods as the x-ray flares. When a geomagnetic storm or SPE was confirmed, the flare event was eliminated as a candidate.

We identified flare candidates using the Hinode catalogue as a starting point (Watanabe et al., 2012). We visualized the potential events using Moller’s (2021) program, which plots x-ray flux using hard x-ray and short x-ray data versus universal time (UT) for a specific space weather event (NOAA, 2020). We then selected flares based on flare class, date, and timing.

Following Schumer (2010), we restricted our analysis to flare times during which the solar zenith angle was less than  $80^\circ$ . This limited the times of interest to roughly 1500 to 2400 UT and eliminated most flares during the winter. Above the M4 flare class, Ogunmodimu et al. (2018) identify a positive correlation between maximum absorption and peak flare intensity. As the intensity of the flare increases, so does the effect on absorption, with X class flares having the largest effect. Therefore, we selected the largest

flares available and eliminated events below the M4 flare class when the effects were not visible in the riometer data. We cross-referenced the x-ray flux activity with the riometer data provided by the University of Calgary (2005) to determine if an absorption event occurred during the timing of the flare candidate.

Solar proton events (SPE) occur when solar energetic particles (SEP) are accelerated either via solar flares, called impulsive events, or from coronal mass ejections (CME) propagating toward Earth, called gradual events. These SEPs can become entrained on magnetic field lines that connect to the Earth's polar caps and precipitate into the atmosphere, increasing ionization rates in the D-region, which leads to HF radio waves becoming absorbed (Rose & Ziauddin, 1962).

The SPE archive was accessed courtesy of the European Space Agency (ESA, 2021) and the open dataset from NASA (NOAA, 2021b). We screened the flare events to identify those that had a simultaneous SPE. Riometer absorption data could potentially be contaminated by a SPE, thus we considered the latitude of the riometer station and the proton energy level to determine if the candidate is usable.

High-energy proton detectors measure proton flux ( $p^+/\text{cm}^2/\text{s}/\text{sr}$ ) for various particle energies: 1 MeV, 5 MeV, 10 MeV, 30 MeV, 50 MeV and 100 MeV. Particle energies less than 30 MeV were assumed to have little impact on the riometer absorption data. We closely examined the riometer data for noise during periods when the particle fluxes at energies greater than 30 MeV were elevated.

High latitude stations showed more noise than the low latitude stations during SPE. If the riometer station is located south of roughly  $70^\circ$  magnetic latitude, we assumed the SPE would not be a contaminant source for the absorption data caused by high energy particles. This is because the polar cap regions are located northward of  $70^\circ$  magnetic latitude and the elevated flux associated with high energy particles traveling to the polar caps can impact HF radio communication by enhancing ionization in the D-region. Most of the 13 NORSTAR riometer stations are located further south (Patterson et al., 2001).

Three of NORSTAR's riometer stations, CONT, ESKI, and RANK, are located close to  $70^\circ$  magnetic latitude with a fourth station, TALO, at  $79.5^\circ$ . For these stations we

assumed a SPE could affect the riometer absorption data, while the southern stations would be mostly unaffected.

The 7 June 2000 event showed elevated proton fluxes at energies less than 30 MeV, and most stations were unaffected. We included data from RABB, CHUR, CONT, MCMU, and ISLL for this event as contamination was not observed at those stations. The high latitude stations TALO, RANK, and ESKI were excluded due to noise.

If an SPE occurred during the timing of the flare candidate, we cross-referenced it with the SPE plot; our goal was to determine if the riometer absorption was noisy during the period and did not correlate to the x-ray flux. Eighteen events were excluded after screening for proton contamination.

Figure 6 provides an example of an SPE event occurring the same day as a solar flare. The 14 July 2000 event was recorded by the TALO riometer station. The station is located at  $79.5^\circ$  magnetic latitude, in a region closer to the polar caps. The TALO riometer would likely pick up absorption contamination during an SPE event due to the proximity. By correlating x-ray flux peaks to absorption peaks, we can attribute the source of absorption to a solar flare. We accomplish this by plotting the x-ray flux data in red on the same axis as the riometer absorption, which is shown in black. To fit on the same plot, the x-ray flux is scaled as

$$300 \times \sqrt{U_{xray}} + Y(Absorption) dB, \quad (8)$$

where the  $U_{xray}$  is the x-ray flux and  $Y(Absorption)$  is the Y-axis starting value, in this case -5 dB. In Figure 6, a solar flare event occurs early on 14 July 2000 between 1000 UT to 1200 UT, with a maximum near 1030 UT. However, the maximum riometer absorption does not occur until between 1400 to 1800 UT. This indicates the absorption over the 1400 to 1800 UT period can be attributed to something other than the x-rays. By comparing the timing of the absorption with the proton activity in Figure 7, we infer the source is an SPE and therefore exclude the event.

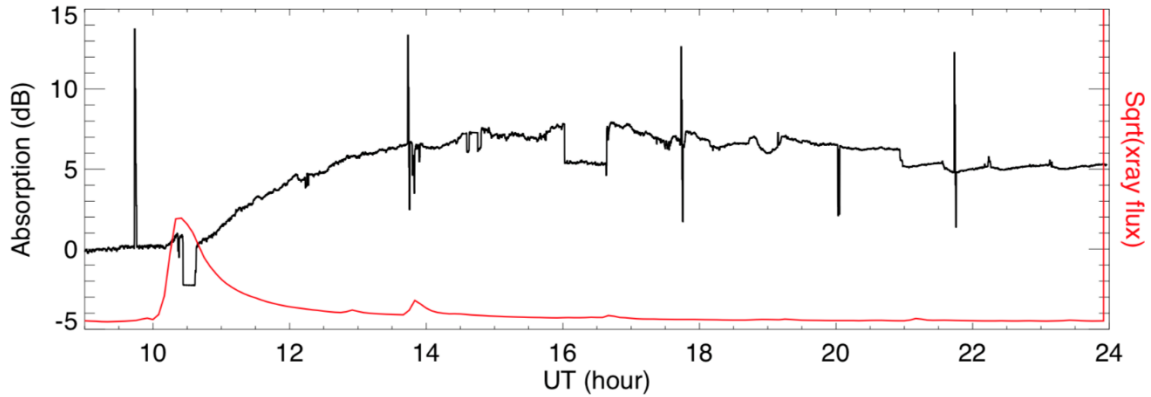


Figure 6. Absorption recorded in decibels by the TALO riometer on 14 July 2000. Adapted from NOAA (2020); University of Calgary (2021). Absorption is plotted in black with the square root of the x-ray flux in red. The plot shows an X5.7 class flare with x-ray flux peak at 1024 UT.

Figure 7 shows a plot of the proton flux corresponding to the event described in Figure 6. As defined by the European Space Agency (ESA), an SPE occurs when the GOES five-minute average flux of protons with energy  $>10$  MeV exceeds  $2.0 \text{ p}^+/\text{cm}^2/\text{s}/\text{sr}$ . ESA considers the SPE over when flux returns to values below  $1.0 \text{ p}^+/\text{cm}^2/\text{s}/\text{sr}$ . The 14 July 2000 event had an elevated flux of particles at energies  $>30$  MeV, which is used as an indicator that absorption recorded by high magnetic latitude riometer stations may be contaminated by the SPE activity. Particle flux was also elevated for energies exceeding 50 MeV and 100 MeV during the same period of the absorption signatures in Figure 6, further suggesting the absorption was due to the SPE. Thus, the absorption can be attributed to an SPE and the 14 July 2000 event was not included among the 101 flare events.

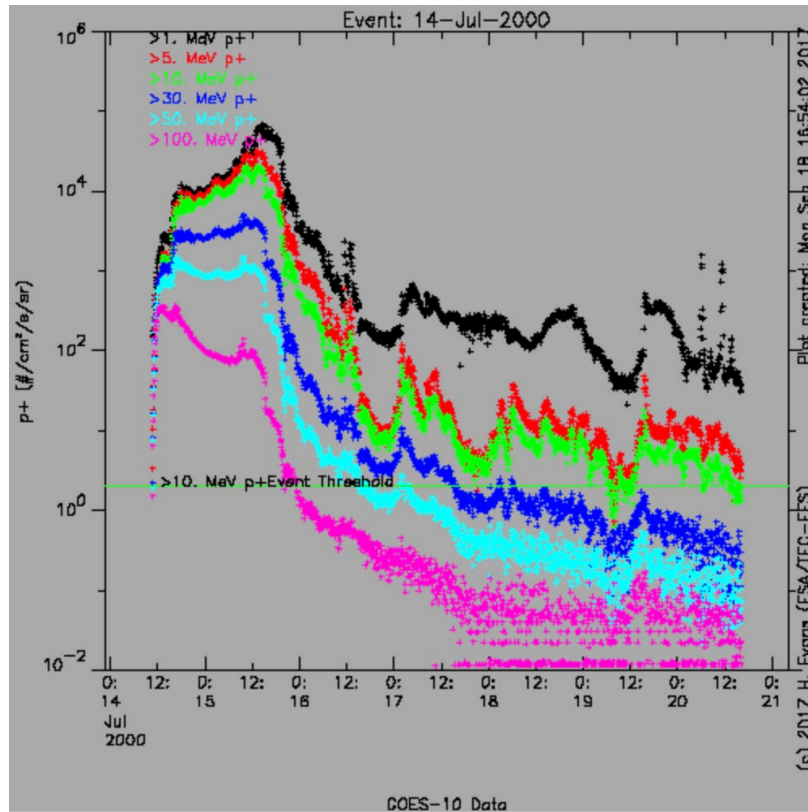


Figure 7. Proton flux measured during the 14 July 2000 event. Source: European Space Agency (2021). The different colors represent the energy of the protons being measured. The black line denotes particles with energy  $>1$  MeV, while the magenta line indicates particles with energies  $>100$  MeV. The horizontal green line represents a threshold established by the European Space Agency to declare a proton event based on the flux of  $>10$  MeV protons.

Because the DRAP Model Validation report (Akmaev, 2010) recommends using well-isolated x-ray flare events, we also established criteria to cross-examine flares of interest with geomagnetic storms to filter them out. Geomagnetic storms occur when energy extracted from the solar wind is explosively released in the tail region of the magnetosphere (NASA, 2020). This energy release accelerates particles that stream down magnetic field lines and are deposited in the high latitude auroral regions. A geomagnetic activity archive was utilized to analyze whether a significant event occurred during the flare period.

The Kp activity index is based on measurements taken from 13 geomagnetic observatories located around the world. The Kp index archive was accessed from (Matzka et al., 2021). The observatories house ground-based magnetometers which measure the deviation of the horizontal component of the magnetic field over a three-hour period. This allows the magnetometers to record a quasi-logarithmic measure of geomagnetic activity that ranges from zero to nine, where nine is an extreme geomagnetic storm.

The space weather storms described above carried into 15 July 2000 where an extreme geomagnetic storm began at 1200 UT and continued into 16 July 2000. Figure 8 shows the riometer absorption data during the event. No enhanced x-ray flux is observed during this period, meaning that the absorption source is not correlated with a solar flare and instead is caused by a different space weather event. The SPE archives from the ESA (2021) and NOAA (2021b) were cross-referenced to examine if proton activity was contaminating the data. The NOAA (2021b) archive notes some lingering proton activity ending at 1230 UT on 15 July 2000. The absorption in Figure 8 begins below 5 dB and gradually rises over a 3-hour period. By 1200 UT the absorption reaches approximately 14.9 dB and remains high until it slightly dips by 1500 UT. The dip returns to 14.9 dB until 1600 UT where it fluctuates then decreases after 1700 UT. The absorption then continues to trend around 10 dB till the end of the period despite the fluctuations.

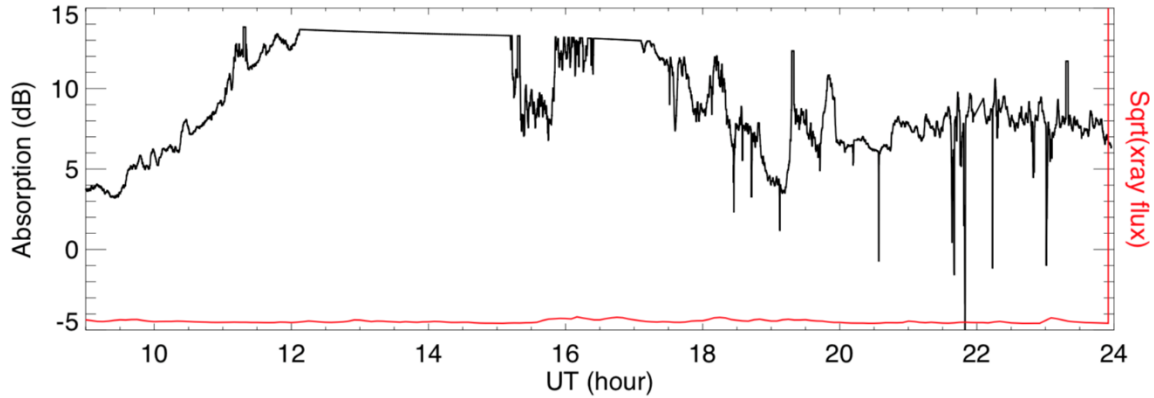


Figure 8. Absorption recorded at the MCMU riometer from 0900-2400 UT on 15 July 2000 during a large geomagnetic storm. Adapted from NOAA (2020); University of Calgary (2021). The signal absorption (dB) at 30 MHz is shown in black. The square-root of the x-ray flux is shown in red. No solar flares are observed during the period.

Figure 9 displays the planetary 3-hour index of geomagnetic activity for a 3-day period. The Kp index ranges from 0-9 and correlates with a color-coded scale that records activity from quiet to extreme. We compared the timing of absorption signatures from Figure 8 to the Kp index in Figure 9 to determine if a geomagnetic storm had occurred during the period. The Kp index shown in Figure 9 indicates that geomagnetic activity also occurs throughout the elevated absorption depicted in Figure 8. The absorption signatures are related to both an SPE and geomagnetic storm. This determination is made based on the timing of the event overlapping with the SPE that started on 14 July and continued into 15 July, where the Kp levels reach above the G1 threshold. The lack of x-ray flux confirms the event is not related to a solar flare. In this manner, we demonstrate how events are eliminated from consideration. Any candidate event with Kp data of G1 or greater would be cut from the list. Had a candidate flare event occurred on 15 July 2000, it could not have been utilized in the model flare list.

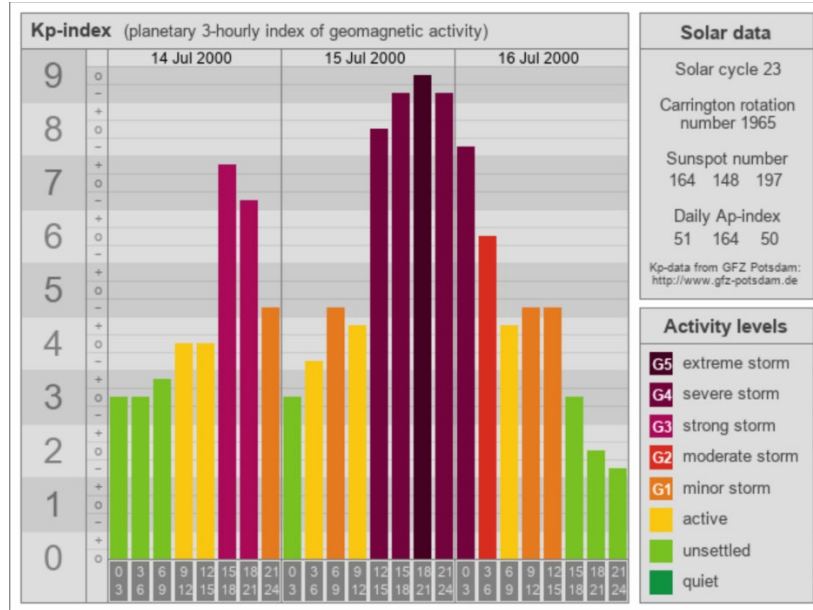


Figure 9. Kp-index for the 15 July 2000 flare event. Source: Thuesner (2021). The activity levels on 15 July 2000 shows a severe level geomagnetic storm (G4) starting at 1200 UT becoming an extreme storm (G5) by 1800 UT. The geomagnetic storm event continues into 16 July 2000 until the activity level quiets down to unsettled by 1500 UT.

To be an ideal flare candidate, the Kp index should not exceed the G1 threshold throughout the event. Though SPE are avoided, if a proton event occurs during the flare, stations south of 70° magnetic latitude can be used as long as noise is not contaminating the data. Figure 10 is an example of flare meeting these criteria. It is noted that none of the archive lists indicate a significant SPE event occurring on 02 April 2001, so an SPE event can be eliminated as a possible source of absorption. The absorption and x-ray flux peaks correlate, with both increasing near 2150 UT. The absorption peaks at 5.8 dB near 2200 UT; the same time the x-ray flux peaks. Both absorption and flux then decrease and return to baseline by 2400 UT. The x-ray flux measured by the GOES satellite on 02 April 2001 corresponds to an X17 class flare ( $1.66 \times 10^{-3} \text{ W/m}^2$ ).

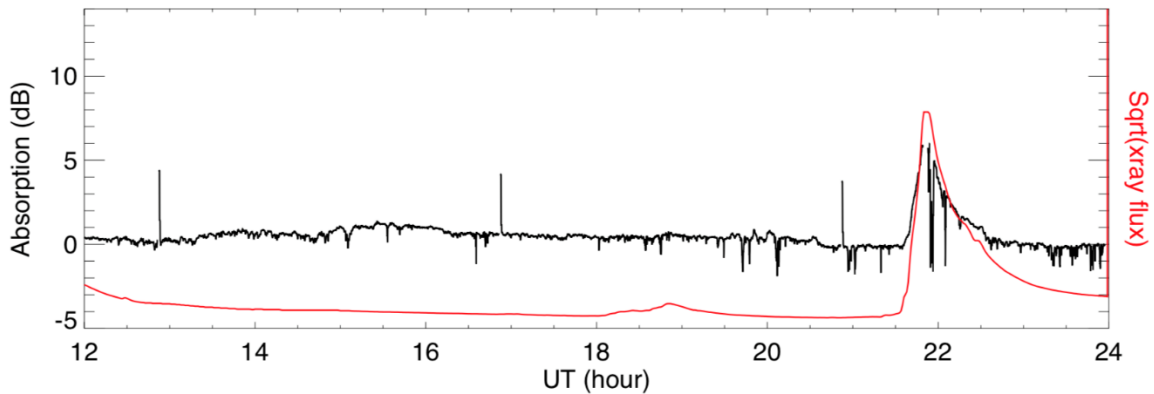


Figure 10. Absorption correlating with x-ray flux during the 02 April 2001 flare event for the ESKI riometer station. Adapted from: NOAA (2020); University of Calgary (2021). Raw absorption is measured in decibels and is depicted by the black line with x-ray flux in red.

Figure 11 shows the Kp levels remain below the G1 threshold during the flare event in Figure 10, which suggests the absorption event does not correspond to magnetic activity. Since SPE is already eliminated as a source of absorption because it was not recorded as a notable event by the archives, the absorption peak can be attributed to a solar flare. The confirmation also comes from the x-ray flux peak occurring during the max absorption within the period. To conclude, the 02 April 2001 absorption can be attributed to a solar flare and provides an example of a flare that would meet selection criteria for this study.

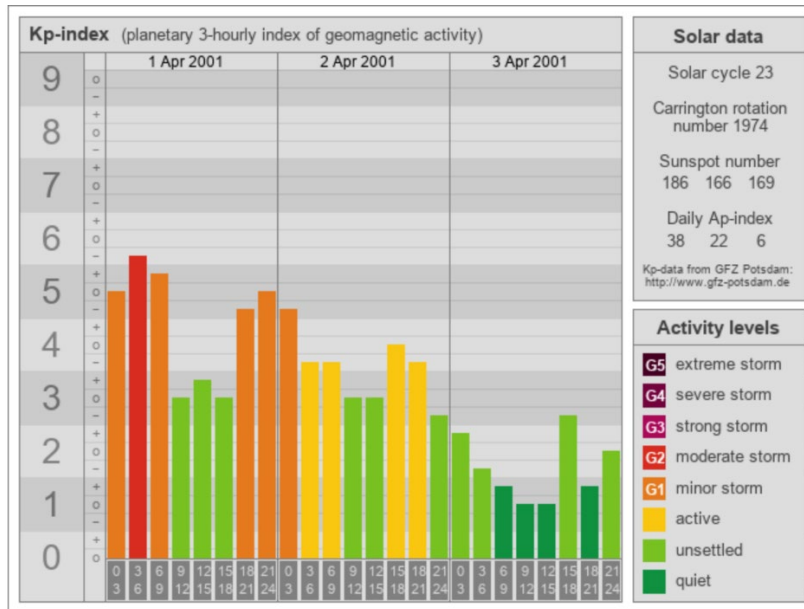


Figure 11. Kp index for the 02 April 2001 absorption event. Source: Thuesner (2021).

Our flare selection criteria eliminated events when the Kp index reached G1 or higher. We avoided flares with proton activity, but if an increase in the energetic proton flux for energies greater than 30 MeV was noted, we primarily used stations south of 70° magnetic latitude to eliminate candidates with potential contamination. If the SPE had proton energies less than 30 MeV and the riometer station was north of 70° magnetic latitude we included the flare if the station did not have noise in the riometer data. 16 flare events were observed by the 13 riometer stations, which after eliminating noise and contamination, resulted in a total of 101 flare events. We divided the usable events into ‘model’ and ‘control’ groups with 39 flares in the model flare list and 62 flares in the control list to observe how the model performs at different stations.

The model list focused on including more ideal X-class flares to optimize the fit parameters with 10 flares that have flux magnitudes greater than  $10^{-3}$  W/m<sup>2</sup>. The model list avoided smaller magnitude flares but did include two flares with M class flux magnitude. The control list expanded on usable flares by adding 36 M class flares with magnitudes ranging from  $10^{-6}$  W/m<sup>2</sup> to  $10^{-5}$  W/m<sup>2</sup>. Both lists had an almost even number of flares with

X class flare magnitudes greater than  $10^{-4}$  W/m<sup>2</sup>, where the model list had 27 X class flares and the control list had 26 X class flares.

The model list and control list are found in Appendices A and B. Both lists include a flare start and end period, and a fit start and end period. The flare start and end columns define the timing of the full duration of the flare event. The fit start and end define the fitting window where the model is applied for an individual flare event. Both lists also include the date of the event and the riometer station code.

## **B. RIOMETER DATA PREPARATION**

The absorption data needed to be manipulated before creating our model to ensure the best possible fit. To match the 1-minute cadence of the x-ray flux data, the riometer absorption data was down-sampled from 12 samples per minute to one per minute, using a median function. The available x-ray data were then paired with the corresponding riometer absorption data. This is done to correlate the absorption and x-ray flux peaks for analysis. Noise spikes and negative absorption values could cause the model to misidentify the maximum absorption and thus needed to be eliminated. This is accomplished by introducing a fitting window and maximum absorption cap. Noise outside of the fitting window would not be included in our model. Because the flux and absorption correlate, we could determine when the max absorption should occur with peaks correlating, as in Figure 10.

It must be noted that radio bursts occur through a large portion of the flare list, causing noise that may contaminate the maximum absorption output. The NOAA (2012a) radio burst archive was used to cross-examine flare peak timing with radio burst noise spikes. The Solar Radio Bursts guide by NOAA (2012b) was used to decode the radio burst archive. Flare selection avoided overlap of radio bursts during peak absorption. The cap was applied to all flare events thus limiting contamination from most noise sources. The cap prevents radio bursts from influencing the initial fit and is unique for each flare event based on the maximum absorption for the event and station. Lastly, the solar zenith angle was calculated during the flare event times; periods when the zenith angle exceeded 80°

degrees were not included in the study to avoid division by values approaching zero (Schumer, 2010).

### C. BASELINE OF RIOMETER ABSORPTION TO ZERO

As discussed previously in Section H, the absorption estimate for each station is found by subtracting a quiet day curve from the measured signal strength. However, an average QDC cannot fully capture the day-to-day variations, so offsets can occur. Having eliminated absorption sources due to SPEs and geomagnetic storms discussed in Chapter III. Section A, we assume all remaining absorption is due only to solar flares and apply a ‘baseline offset’ to force the absorption to zero as the x-ray flux goes to zero. This is accomplished by fitting a curve to the absorption data and subtracting any resulting offset.

To calculate the baseline offset, the flare-time absorption for each station is fit with a function of the form  $y = a + bx^c$ , where  $x$  represents the x-ray flux in  $\text{W/m}^2$  and  $y$  is the absorption in decibels. The terms  $a$ ,  $b$ , and  $c$  are fitting parameters. We used an initial guess of  $a = 0$ ,  $b = 1334.25$ ,  $c = 0.67$  based on prior (iterative) fitting. The resulting fit value for parameter  $a$  then provides the baseline offset for the flare event of interest and is unique for each case. The offset value  $a$  is subtracted from the flare-time absorption for the station. This process is repeated for all stations and events individually.

Figure 12 illustrates how the fitting works using the baseline offset technique. First the raw absorption data is fit with the function described to determine the offset amount  $a$ . The absorption is then shifted to the baseline and re-plotted. Figure 13 shows how the offset is calculated for the flare event in Figure 12 and is further discussed below.

The 7 June 2000 flare event in Figure 12 is an X1.3 class flare ( $1.28 \times 10^{-4} \text{ W/m}^2$ ) from the control list and is baselined to zero. A large noise spike in absorption exceeding 4 dB occurs at the decimal time 15.1 UT. The absorption is at the baseline until the absorption increases at roughly 15.5 UT and reaches a maximum of 2.4 dB peak at 15.86 UT. Setting the absorption cap parameter is not necessary since the noise spike is outside of the fit window. In this case, the raw absorption depicted in black on Figure 12 is shifted down to baseline by 0.6915 dB, a value calculated in Figure 13.

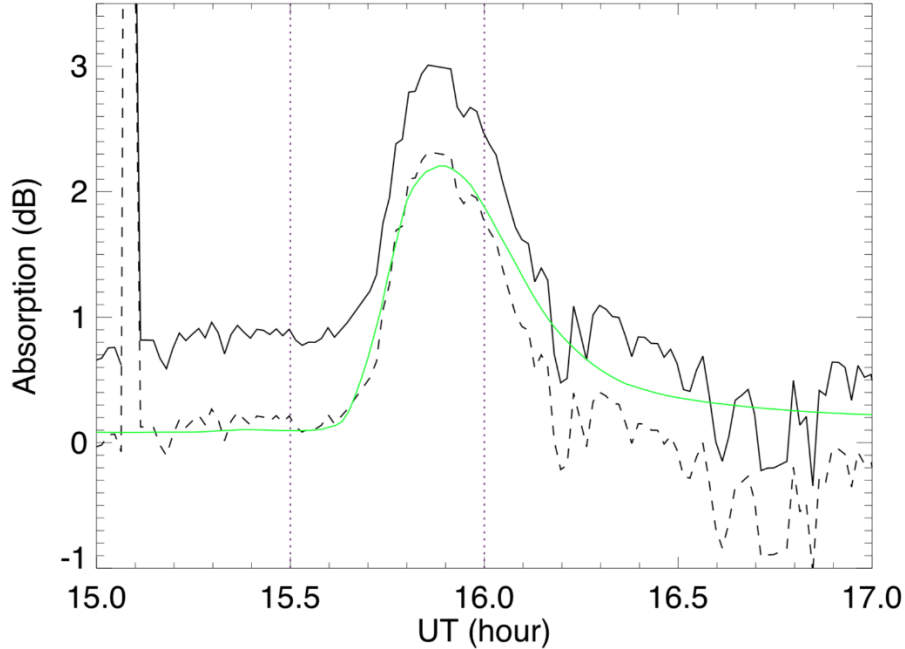


Figure 12. The baselined absorption measured at ISLL observatory on 7 June 2000. Adapted from NOAA (2020); University of Calgary (2021). The black line depicts the raw measured absorption. The green line shows a fit to the raw data with the baseline subtracted. The vertical dashed lines represent the fit range. The baselined data is depicted by the dashed line.

Figure 13 shows the absorption values from the 7 June 2000 event as a function of x-ray flux. The red data points plot the raw absorption, which is then fit using the functional form  $y = a + bx^c$  to produce the red curve and displayed equation. The fitting coefficient  $a$  is subtracted from the raw data resulting in the blue data points, which are offset to zero.

The equation shown in Figure 13 is the fit of the absorption in decibels to the x-ray flux in  $\text{W/m}^2$  for the 7 June 2000 flare at ISLL. The equation inputs x-ray flux for the  $x$  value and the output  $y$  gives absorption. The fitting equation gives values for  $b = 876.24$  and  $c = 0.67$  which are the unique fit parameters for this event. The offset  $a$  is calculated to be 0.6915 dB. The difference between the red data points and the blue points represents the amount that was offset to reach the baseline. In this example, the fit considers data between the decimal time 15.5 UT and 16.0 UT, which covers most of the flare period through the duration of the maximum but avoids noise later in the flare.

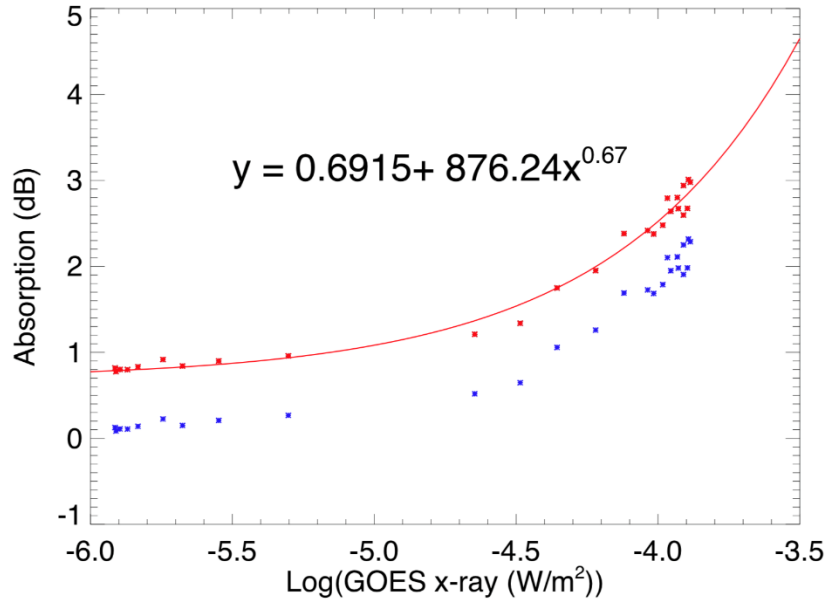


Figure 13. The 07 June 2000 flare event recorded by the ISLL riometer station showing absorption as a function of x-ray flux. Adapted from NOAA (2020); University of Calgary (2021). The red data points show the raw absorption, which is then fit using the functional form  $y = a + bx^c$  to produce the red curve and displayed equation. The fitting coefficient  $a$  is subtracted from the raw data resulting in the blue data points, which are offset to zero.

A large offset amount, like the one shown in Figure 12 and Figure 13, demonstrates the importance of performing the baseline offset technique. Some flare events had a greater amount of spread between the raw and baselined absorption. This would cause the fit performance to degrade when the fitting coefficient  $a$  was large. When compared to a flare with little to no noise spikes or other contamination sources that had calculated a small amount for the fitting coefficient  $a$ , the fit performance would significantly improve. Figure 14 serves as an example of a flare that required only a relatively minor adjustment to baseline the data and is considered a clean flare since it has no significant noise or contamination sources. The X1.8 class flare ( $1.8 \times 10^{-4} \text{ W/m}^2$ ) occurring on 15 July 2004 plots the raw and baselined absorption. Repeating the steps outlined in Figure 12 and Figure 13, the raw absorption is fit using the functional form  $y = a + bx^c$ , where the fitting coefficient  $a$  is then subtracted from all the raw data to baseline the absorption. The absorption begins to increase near the decimal time 18.3 UT, peaks at 2.49 dB near 18.4

UT then gradually decreases as it approaches 19.2 UT. The baselined absorption is then fit in the form  $y = bx^c$ .

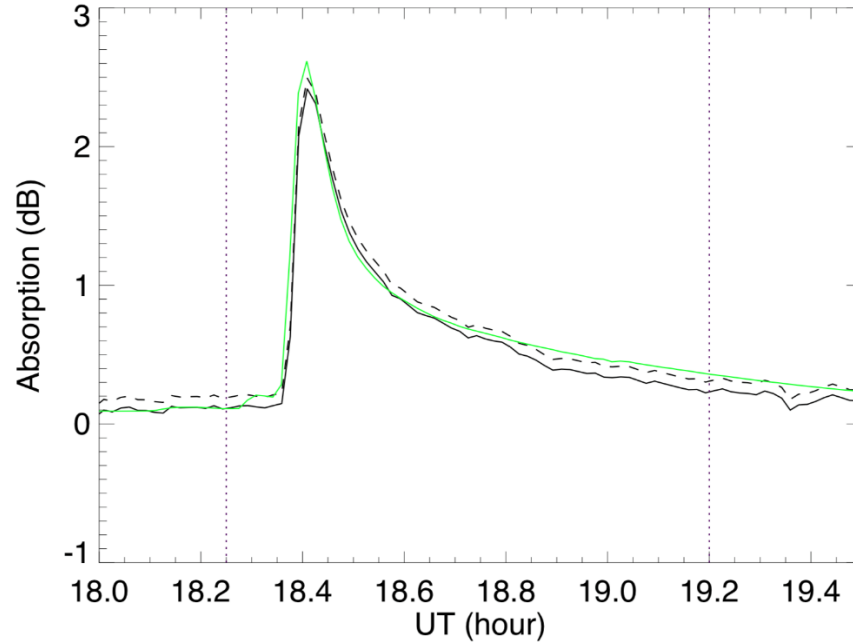


Figure 14. The baselined absorption measured at the RANK station on 15 July 2004. Adapted from NOAA (2020); University of Calgary (2021). The black line depicts the raw measured absorption. The green line shows a fit to the raw data with the baseline subtracted. The vertical dashed lines represent the fit range. The baselined data is depicted by the dashed line.

Figure 15 calculates the fit equation that determines the amount to be offset for the event in Figure 14. Similar to Figure 13, Figure 15 shows the result of the initial fit using the form  $y = a + bx^c$  seen as the red curve and plots absorption as a function of the log of the x-ray flux. The fitting coefficient  $a = -0.077$  dB is subtracted from the raw absorption data points in red. The offset to zero results in the blue data points. The magnitude of the baseline offset  $a = -0.077$  dB, is smaller than the value found in Figure 13 where the initial fit equation gives a much larger baseline offset of 0.6915 dB. The variation in offset magnitude demonstrates the necessity to baseline the absorption to prepare the flare events for model development.

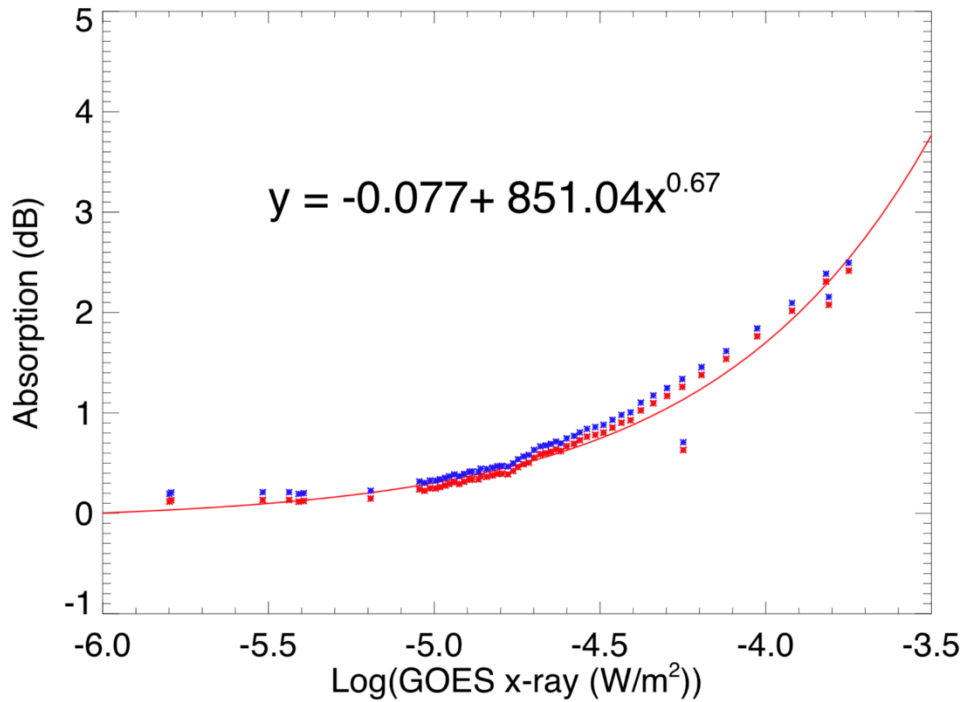


Figure 15. The 15 July 2004 flare event recorded by the RANK riometer station showing absorption as a function of x-ray flux. Adapted from NOAA (2020); University of Calgary (2021). The red data points show the raw absorption, which is then fit using the functional form  $y = a + bx^c$  to produce the red curve and displayed equation. The fitting coefficient  $a$  is subtracted from the raw data resulting in the blue data points, which are offset to zero.

The median offset for the model list was found to be 0.223 dB with a maximum of 0.6915 dB. For the control list, the median was 0.144 dB, and the maximum offset was 0.413 dB. The model list included flares with larger magnitudes, which likely led to larger offset values than the control. The standard deviation for the model list was found to be 0.15 with the standard deviation of the control list equal to 0.12. The standard deviations for both lists are low and are within  $\pm 0.3$  of each other.

## IV. MODEL CREATION

We develop a statistical regression model, using x-ray flux and solar zenith angle as predictor variables, to determine the HF radio absorption during solar flares. We avoided overfitting in the regression by including a large sample size with over 100 events. A scatter plot of the normalized absorption data is used to establish the overall pattern of the data. We form the regression by adjusting a normalization coefficient and model output parameters then fitting it to the plot. Root mean square error (RMSE) is used to verify the best fit and select the final model parameters. We validated the performance of our model and two existing models again using RMSE and analyze the predictive trends of each. Our new model is found to perform better at predicting the HF radio absorption than the existing models. Lastly, we apply our model to a case study of an extremely large X class flare.

### A. NORMALIZING PREDICTED ABSORPTION TO DEVELOP A MODEL FRAMEWORK

In the previous chapter we described how to determine and baseline the riometer absorption data for each station. The results are a time-series of absorption measurements as a function of the x-ray flux. However, from Equation (3) we know the absorption is proportional to the electron density, which depends not only on the x-ray flux, but also on the solar zenith angle. Since the measurements for each solar flare event occur at different stations (locations) and times, the solar zenith angle will also be different. In this section we describe a technique to normalize for the solar zenith angle dependence. Having completed this normalization, we can then plot all of the absorption measurements as a function of x-ray flux and generate our statistical regression.

The normalization technique is described by

$$\frac{Y_{predicted}(U_{Xray}, \chi)}{\cos^r(\chi)} = A \cdot U_{Xray}^B \quad (9)$$

First, we normalize the absorption data  $Y_{predicted}(U_{Xray}, \chi)$  by  $\cos^r(\chi)$  before the fit, where  $\chi$  is the solar zenith angle. The  $\cos^r(\chi)$  normalizes absorption in relation to the solar zenith angle since the absorption decreases for locations away from local noon. The location of

maximum absorption occurs where the Sun is directly overhead, which is termed the subsolar point. The normalized absorption from Equation (9) assumes absorption goes to zero as x-ray flux goes to zero, which was enforced using the baseline technique described in Chapter III, Section C. The regression parameters  $A$  and  $B$  are calculated for a specific normalization coefficient  $r$ , and  $U_{Xray}$  represents real-time x-ray flux.

Figure 16 shows the normalized absorption and x-ray data for all 101 events from the model list and is an example of the fit using a specific normalization coefficient of  $r = 1$ . The fit in Figure 16 has few outliers, as all the riometer station data tightly groups to follow the curve. A poor fit would be represented by a larger scatter and lack of tightness from the normalized absorption and x-ray flux data. The normalization coefficient  $r = 1$  gives model output values  $A = 815.567$  and  $B = 0.64$  yielding a model equation of  $y = 815.567x^{0.64}$  where  $y$  is the normalized absorption value and  $x$  is the known x-ray flux.

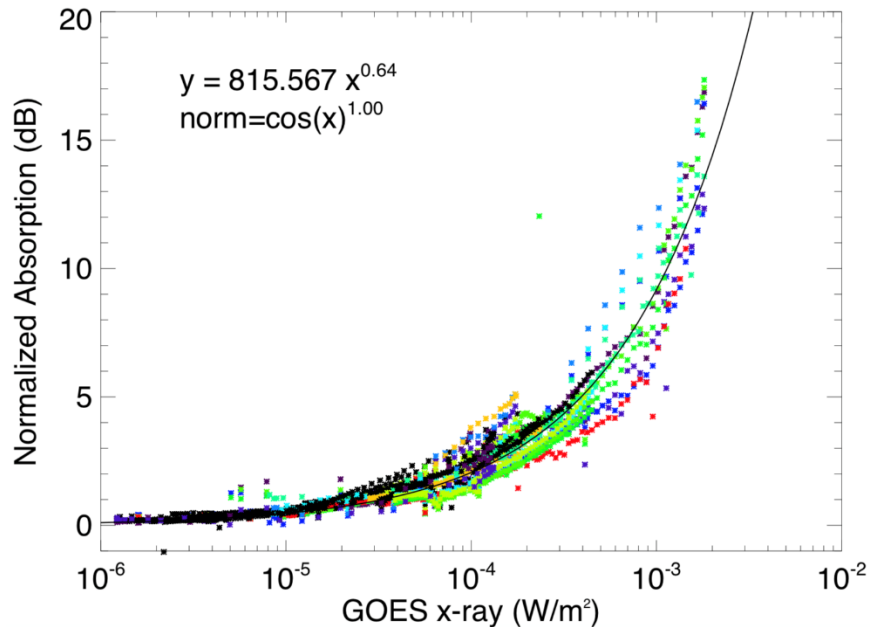


Figure 16. Our model is applied as a fit to the normalized absorption versus x-ray flux data. Adapted from NOAA (2020); University of Calgary (2021). Our model is depicted by the black line. The data is scattered per station and are represented by a different color.

The normalization allowed us to remove the solar zenith angle dependence. After generating our model fit from the absorption measurements as a function of x-ray flux, as in Figure 16, we then apply Equation (10) to represent how the model is used to predict the absorption for known x-ray flux and solar zenith angle.

$$Y_{predicted}(U_{Xray}, \chi) = A \cdot U_{Xray}^B \cos^r(\chi), \quad (10)$$

where  $\cos^r(\chi)$  occurs directly on the model equation now that  $\chi$ ,  $A$ , and  $B$  are known parameters,  $r$  represents the normalization coefficient, and  $U_{Xray}$  is the real-time ionizing x-ray flux which is also known.

Each normalization coefficient  $r$  and corresponding model parameters were tested and plotted like the example in Figure 16. We used  $r = 0.75$  from the DRAP and  $r = 0.9$  from the EHA to test the efficacy of each normalization coefficient to find the best result. We also expanded the range up to  $r = 1.5$  to analyze alternative model coefficients for use.

An RMSE test is used to determine a final model by evaluating the predictive capability for different values of the normalization coefficient  $r$ , and model parameters  $A$  and  $B$ . The RMSE is calculated by

$$RMSE = \sqrt{\frac{\sum_{i=1}^n (Y_{measured} - Y_{predicted})^2}{n}}, \quad (11)$$

where  $n$  is the sample size. In Equation (11), the model output from Equation (10) represents  $Y_{predicted}$  and the time-series of baselined absorption values (described in Chapter III, Section C) represents  $Y_{measured}$ .

The normalization coefficients, model outputs, and RMSE are summarized in Table 4. Model outputs  $A$  and  $B$  are used to create model candidates for different values of  $r$ . The model using the  $r = 0.75$  normalization coefficient results in the largest RMSE; recall the DRAP model uses a normalization coefficient of 0.75. The EHA coefficient of  $r = 0.9$  has the second largest RMSE. The  $r = 1.0$  normalization coefficient performs best with the lowest RMSE value 0.267 dB. The normalization coefficient value of  $r = 1.1$  shows that

RMSE begins to rise for values higher than  $r = 1.0$ . The fitting demonstrated degraded performance past the  $r = 1.5$  value.

Table 4. Model fits for different normalization coefficients,  $r$

Normalization Coefficient	Model Output A	Model Output B	RMSE
0.75	363.3	0.5793	0.293
0.9	592.3	0.6221	0.273
1.0	815.6	0.6496	0.267
1.1	1115	0.6761	0.270
1.2	1512	0.7012	0.283
1.3	2031	0.7251	0.308
1.4	2702	0.7474	0.345
1.5	3557	0.7682	0.395

Based on the RMSE results in Table 4, we selected the model candidate with  $A = 815.6$ ,  $B = 0.65$ , and  $r = 1.0$ . Our final model is therefore given by

$$Y_{predicted}(U_{Xray}, \chi) = 815.6 \cdot U_{Xray}^{0.65} \cos^{1.0}(\chi), \quad (12)$$

where  $U_{Xray}$  is the x-ray flux and  $\chi$  is the solar zenith angle.

## B. COMPARISON OF MODELS

We first compare the DRAP, EHA, and our model's performance by examining a few specific examples to demonstrate the general behavior of the models and draw conclusions of model bias. The first example uses an X class flare from the model list and shows the data preparation techniques outlined in Chapter III in action. The second example considers an M class flare from the control list to represent how the models performed for the relatively smaller M class flares. Finally, the last example examines a larger magnitude X class flare to conclude which model has the best predictive capability for the largest flares, while further illustrating each models' biases. Final conclusions on predictive performance are made using RMSE. These examples only serve to illustrate the

general trends: the EHA overpredicts, the DRAP underpredicts, and our model performs best overall.

Figure 17 applies all three models to an X1.8 class flare ( $1.8 \times 10^{-4} \text{ W/m}^2$ ) from the model list. The fit window covers the decimal period from 18.25 UT to 19.20 UT. A large noise spike is observed right after 18.8 UT. A cap of 2.6 dB was applied during the initial fitting to keep the noise spike from interfering with our model's prediction of the maximum peak. Our model closely predicts the maximum absorption to be 2.5 dB. The EHA overestimates the maximum absorption, predicting 4.0 dB and the DRAP underestimates the maximum, predicting 0.7 dB.

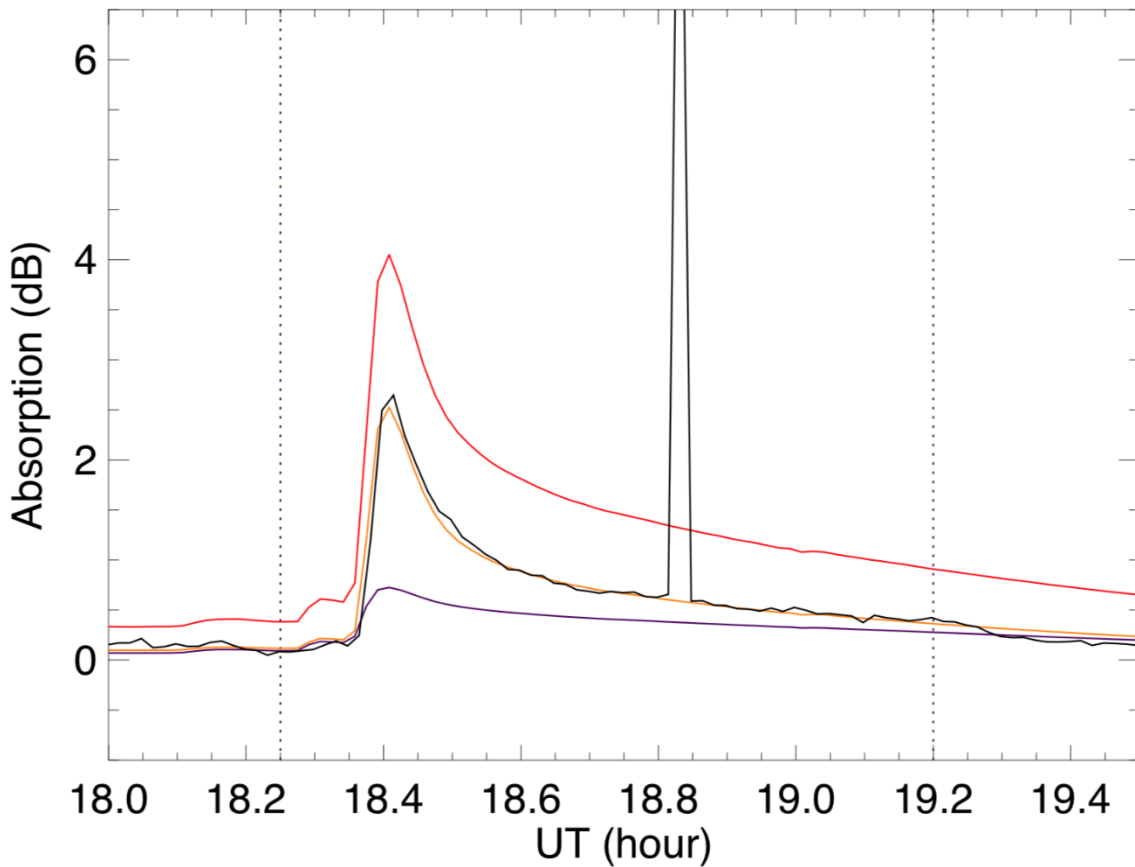


Figure 17. Absorption (black line) recorded at the ISLL observatory during a solar flare on 15 July 2004 from the model list. Adapted from NOAA (2020); University of Calgary (2021). The fit window is represented by the vertical dashed lines. Model predictions are shown in orange (this work), purple (DRAP), and red (EHA).

Figure 18 shows an M6.8 class flare ( $6.75 \times 10^{-5} \text{ W/m}^2$ ) from the control list as observed at the RANK station on 13 July 2004. The DRAP model identifies the first M class flare absorption peak that occurs near 18.6 UT with a prediction of 0.3 dB, matching the observed absorption. However, the DRAP underpredicts the M class peak that occurs at 19.55 UT, predicting only 0.5 dB where the observed absorption is 1.0 dB. The EHA again overestimates the absorption, predicting 2.2 dB. Our model predicts 1.1 dB, closest to the observed absorption. In general, the DRAP tended to underpredict the absorption from M class flares while the EHA overpredicted the absorption.

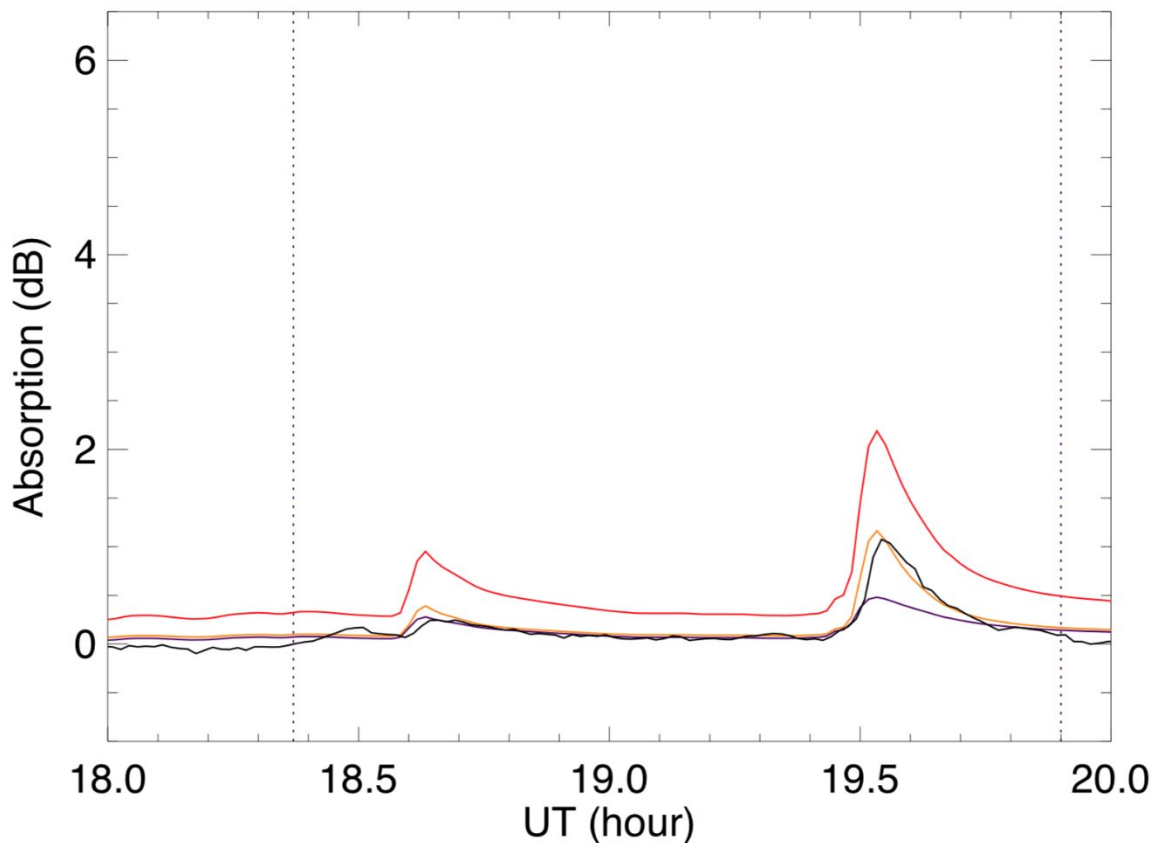


Figure 18. Comparison of predictive performance for the 13 July 2004 control list flare event at RANK riometer station. Adapted from NOAA (2020); University of Calgary (2021). The fit range is represented by the vertical dashed lines and covers the 18.4 UT to 19.9 UT period. Model predictions are shown in orange (this work), purple (DRAP), and red (EHA).

Figure 19 applies all three models to a larger magnitude X17 ( $1.7 \times 10^{-3} \text{ W/m}^2$ ) flare from the model flare list. The fit window covers the period 21.5 UT to 22.85 UT. The observed absorption at the peak of the flare is 4.4 dB, while the EHA model predicts a maximum of 5 dB. Though the EHA overestimates by a smaller margin for this case. Our model prediction came the closest, estimating 4 dB. The DRAP struggles at the 30 MHz frequency, with the model predicting only 0.3 dB of absorption. After analyzing all events, our model most closely predicts the largest class of flares ( $>10^{-3} \text{ W/m}^2$ ).

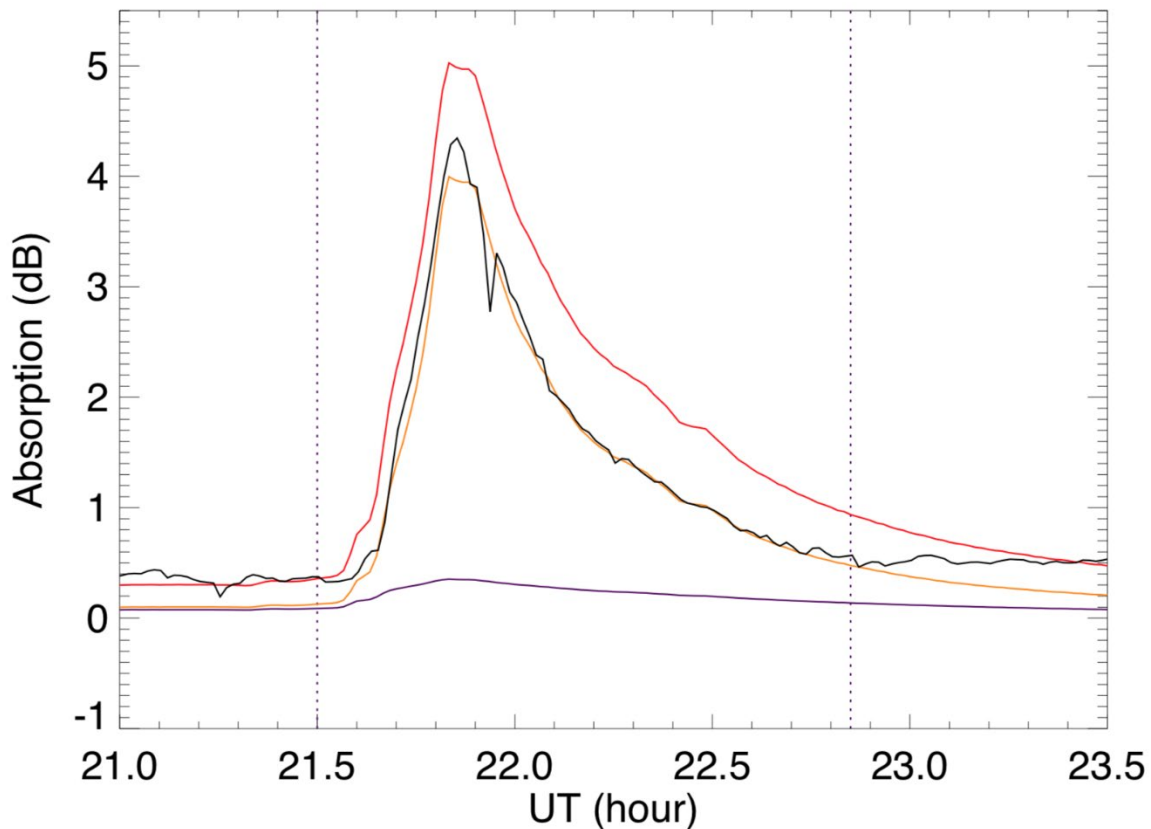


Figure 19. The 2 April 2001 flare event at the TALO observatory. Adapted from NOAA (2020); University of Calgary (2021). The fit range is represented by the vertical dashed lines from 21.5 UT to 22.85 UT. Our model is in orange, the EHA in red, and the DRAP in purple.

These examples demonstrate a trend seen across all 101 events, where the EHA model is overestimating absorption, the DRAP is underestimating absorption, and our model predicts closest to the observed value.

While cases from both lists were used here as examples, we tested the predictive performance of the models by calculating the RMSE for each applied to the model list. We verified the results by calculating RMSE from the control group. The results are discussed in the next section.

### C. RMSE COMPARISON

Chapter IV, Section B provided a method of visualizing the performance of the EHA, DRAP, and our model for specific events. Here we calculate RMSE for the models using both flare lists to evaluate which provides the overall best estimate of absorption. RMSE was calculated using Equation (11), where each model was input as  $Y_{predicted}$ . The results of the calculation are summarized in Table 5.

Table 5. RMSE comparisons between the models.

<b>Model</b>	<b>Model List RMSE (dB)</b>	<b>Control List RMSE (dB)</b>
Our Model	0.267	0.205
EHA	0.862	0.879
DRAP	1.007	0.726

Our model has the lowest RMSE compared to EHA and DRAP for both the model and control lists, indicating the model performed best for the events at 30 MHz for the midlatitude riometers. Our model performed slightly worse for the model list, which was used to generate the fit. This was potentially due to the model list having a greater amount and larger magnitude X class flare events. The EHA model has a slightly lower RMSE than the DRAP for the model list, but the DRAP outperforms the EHA on the control list. Since the model list contains proportionally more X class flares than the control list, this suggests the EHA performs better than the DRAP for large flares (model list), while the DRAP does better for smaller flares (control list). The EHA consistently overpredicts the absorption and the DRAP consistently underpredicts, the DRAP performs better when the flares are small and the EHA when the flares are large. This also suggests that optimizing the frequency scaling factor and normalization coefficient may significantly improve accuracy

for forecasting absorption at higher signals. The EHA was built considering this optimization to improve the predictive capability of real-time HF induced absorption. Our model then further optimized the normalization process outlined by Schumer; thus, our model performs most effectively for M and X class flares at 30 MHz for the midlatitude stations.

#### **D. HALLOWEEN FLARE**

Finally, we apply our model to the famous “Halloween storms” from 19 October to 7 November 2003. The geomagnetic storms during this period caused transformer failures all over Northern Europe with system outages and severe blackouts (NOAA, 2004). NASA officials issued flight directives for astronauts to shelter, and airlines suspended travel in high latitude areas to avoid communication blackout and the high radiation levels associated with an SPE during this time. The most extreme flare occurred on 4 November 2003; it was so large it saturated the sensors, topping out the recorded magnitude at X17.4. NOAA estimated the peak flux reached a magnitude of X28 (NOAA, 2004; Woods et al., 2004).

Many researchers have used different techniques to estimate the flare size of the 4 November 2003 event. Thomson et al. (2004) estimated a magnitude of  $X45 \pm 5$  using sudden phase anomalies of VLF transmission. Brodrick et al. (2005) analyzed CNA in 20.1 MHz riometer data and suggested the flare could have ranged from X34 to X48 in size, with the best fit being X40 in magnitude. Tranquille et al. (2009) examined the observations from the Gamma-Ray Burst experiment (GRB) established by the Ulysses launch in 1990. These observations allowed Tranquille et al. (2009) to create a scaling law by relating the normalized maximum count rate from the GRB experiment to the intensity of the flare given by the GOES data. Tranquille et al. (2009) classified the flare as  $X24.8 \pm 12.6$ . Cliver and Dieterich (2013) noted the estimate is consistent with the work of Kiplinger and Garcia (2004) who predict X30.6 by comparing flares that exhibited similar time profiles to reconstructed light curves for the flares. Cliver and Dieterich (2013) estimated the 4 November 2003 flare to be  $X35 \pm 5$  by using the mean value from the X25-45 estimates and assign uncertainty of  $\pm 5$ .

Our model can be used in reverse to predict the x-ray flux given the observed absorption. Since our model outputs absorption, we can apply it as a known variable to the fitting equations like those displayed in Figure 13 and Figure 15. The 4 November 2003 flare event has a fitting equation for each riometer station, simply solving for the variable  $x$  gave the x-ray flux. We automated the calculation of x-ray flux and superimposed the expected peak. Figure 20, is an example of this process and shows our model's prediction for the 4 November 2003 flare event at the FSMI observatory. The fit range covers the decimal time from 19.55 UT to 20.90 UT. At 19.70 UT the x-ray sensor saturates at  $1.81 \times 10^{-3} \text{ W/m}^2$  flux until 20.08 UT, where the flux decreases. Using the absorption data from the FSMI observatory, our model predicts the x-ray flux should reach X57 ( $5.7 \text{ mW/m}^2$ ) at its maximum.

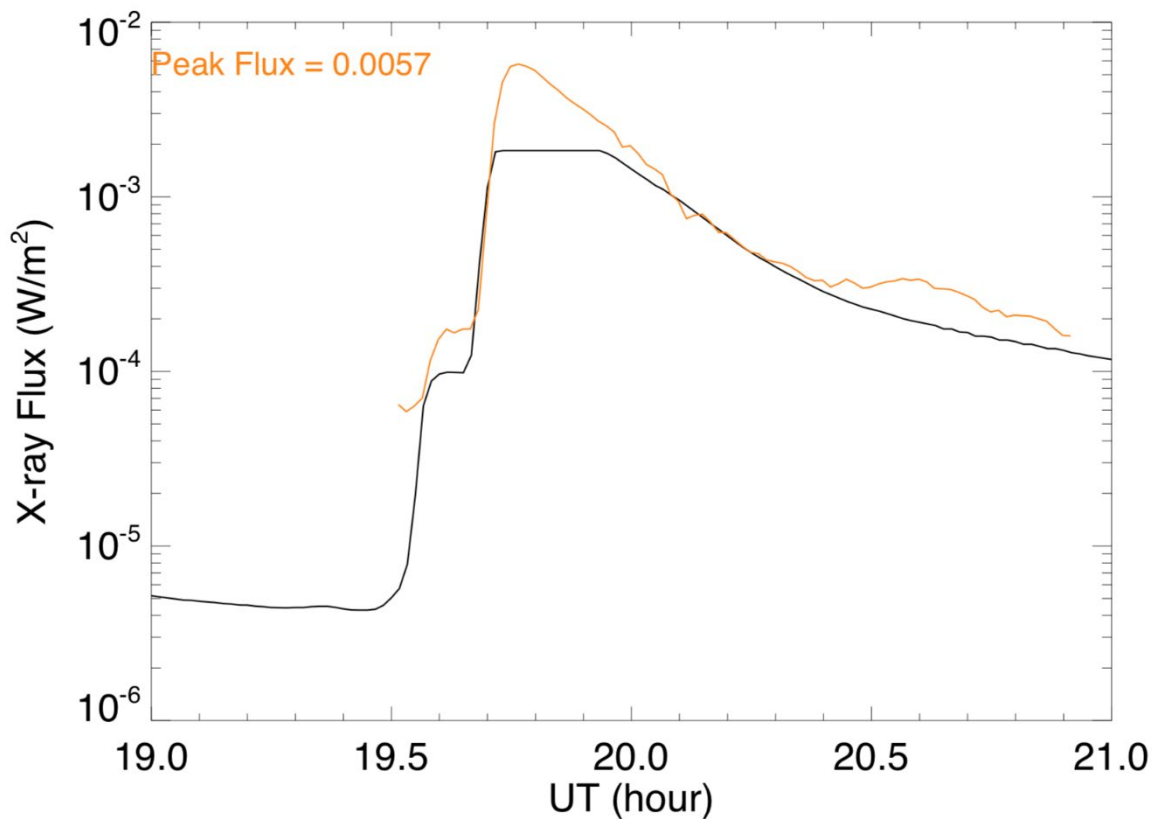


Figure 20. The 04 November 2003 flare at FSMI observatory during the Halloween storms. Adapted from NOAA (2020); University of Calgary (2021). The measured x-ray flux data is in black with our model in orange.

We then applied our model to the riometer stations listed in Table 6 using the same approach depicted in Figure 20. The predicted flare magnitude values range from X38 to X57. Brodrick et al. (2005) found a lower bound for the flare to be X34 ( $3.4 \text{ mW/m}^2$ ), which exceeds the X28 flare size prediction by NOAA (2004). Brodrick et al. (2005) predict an upper range of  $X45 \pm 5$  ( $4.5 \pm 0.5 \text{ mW/m}^2$ ), in agreement with the work of Thomson et al. (2004). Our results range from X38 to X57; the lower range value is consistent with the findings of Brodrick et al. (2005), but the upper value is significantly higher than the Thomson et al. (2004) and Brodrick et al. (2005) predictions.

Table 6. Predicted magnitude for the 04 November 2003 flare.

<b>Riometer Station</b>	<b>Predicted Magnitude</b>
GILL	X38
CHUR	X39
RABB	X54
FSMI	X57
DAWS	X43

Averaging our results for each of the five stations gives an estimated magnitude of  $X46 \pm 8$ , which exceeds the Brodrick et al. (2005) weighted average of X40 but is consistent with the results of Thomson et al. (2004) who estimated a magnitude of X45 and is significantly higher than the initial NOAA estimate of X28 (NOAA, 2004).

THIS PAGE INTENTIONALLY LEFT BLANK

## V. CONCLUSION

Solar flares can cause widespread impacts on communication used for military operations, aviation navigation, and disaster relief efforts. It is important for decision makers and planners to mitigate these impacts by applying real-time flare induced HF absorption models.

Currently, the DRAP is the leading model that government agencies use to monitor flare-induced radio absorption, which is why improving its performance is critical for future warfighting efforts. The DRAP currently scales frequency by  $f^{-1.5}$  and the zenith angle by  $\cos^{0.75}(\chi)$ . Despite recent improvements, our work shows the DRAP underpredicts absorption for large X class flares, based on measurements made using midlatitude riometers at the 30 MHz frequency.

Akmaev (2010) optimized the DRAP model's scaling factors and recommends further work needs to focus on well-isolated flares that exclude geomagnetic storm and SPE activity which was the focus of this research. To do so, our work used the Kp index to exclude geomagnetic storm events and the SPE archives to exclude SPE events from contaminating the absorption data. A threshold for Kp index of G1 or higher was used to eliminate flare candidates contaminated by a geomagnetic storm event. Proton flux associated with energies below 30 MeV were determined to not have a significant impact on the absorption data. We checked each flare candidate to see if there were overlapping periods when particle fluxes were elevated for energies greater than 30 MeV. Riometer stations with proton flux activity north of  $70^\circ$  magnetic latitude were carefully considered, as high energy protons would be a potential source of contamination in the polar cap regions. We then compared the riometer absorption data to the SPE plots to determine if noise interfered with the absorption peak and x-ray flux peak timing and if so, eliminated the flare candidate.

After the riometer data preparation, the raw absorption was offset using the baseline technique. The technique assumed that as x-ray flux approaches zero, so does the absorption. Thus, if there is no contamination by geomagnetic storm or SPE events, then

the absorption is attributed solely to the x-ray flux associated with solar flares. This was accomplished by fitting a curve to the data and subtracting the offset amount. The results of the control list effectively verified the application of the baseline technique confirming that offsetting the absorption is necessary to introduce a better fit. The results of the technique created a time-series of absorption measurements as a function of the x-ray flux.

After the offset was applied, we normalized the predicted absorption. This was done by assuming absorption is proportional to electron density, and thus dependent on the x-ray flux and solar zenith angles. After normalizing for the zenith angle dependence, the time-series of absorption measurements as a function of x-ray flux are plotted, giving rise to our model. Specifically, normalization occurs by scaling the solar zenith angle by  $\cos^r(\chi)$  where the coefficient gave unique model output values for  $A$  and  $B$ , which are used to develop our model's framework. RMSE is used to determine the best performing normalization coefficient and corresponding model  $A$  and model  $B$  values. We found that a normalization coefficient  $r = 1$  with model parameters  $A = 815.6$  and  $B = 0.65$  provide the best performing model,  $Y_{predicted}(U_{Xray}, \chi) = 815.6 \cdot U_{Xray}^{0.65} \cos^{1.0}(\chi)$ .

We then applied RMSE to compare the performance of the DRAP, EHA, and our model. The calculation revealed that our model had the lowest RMSE of 0.267, with the DRAP having the largest value, 1.007, and the EHA performing slightly better with an RMSE of 0.862. Thus, our model outperforms the DRAP and EHA models at the 30 MHz midlatitude stations for all X class flares on the model and control lists. Our model also performs well for predicting M5 class flares, but the DRAP had a few instances where it performed better for lower-class flares. It is posed that optimizing the frequency scaling factor and the normalization coefficient may improve the accuracy for forecasting absorption at higher frequencies.

We applied our model scheme to estimate the size of the famous flare that occurred on 4 November 2003 when the flux saturated the GOES detectors. The initial estimate for the flare magnitude was X28. We found that our model predicted a flare magnitude of  $X46 \pm 8$ , which is close to the X45 and X40 estimates of Thomson et al. (2004) and Brodrick

et al. (2005) respectively. The similarity in predictions helps validate the performance of our model.

Tsiftsi and De La Cruz (2018) apply extreme value theorem to predict that the next Halloween flare sized event would be due to occur every 38 years, thus the next Halloween storm-like event would be due to occur by 2042. It becomes critical that flare induced HF absorption modeling improves before then to mitigate impacts for national security.

Further research could be done to expand and validate our model against data from other riometer networks. By utilizing data from other frequencies researchers could validate the frequency scaling and normalization coefficient's role in optimization. We recommend the SWPC update the DRAP to match our model's scaling and normalization to improve predictions at the 30 MHz frequency for the midlatitudes.

THIS PAGE INTENTIONALLY LEFT BLANK

## APPENDIX A. MODEL FLARE LIST

Appendix A contains all the flare events of the model list, essentially the ‘experimental’ group of flares. Flares are listed by start time and date. Start and end time capture the full period of the flare in universal time with hours and minutes converted to decimal hours. The fit start and end columns also use decimal time and represent the timing captured by the fitting window for our model’s application of the initial fit. Finally, flare events are listed out by riometer station code.

Flare YYYY	Month MM	Day DD	Start Decimal Hours	End Decimal Hours	Fit Start	Fit End	Station ID
2004	7	15	18.00	19.50	18.25	19.20	PINA
2004	7	15	18.00	19.50	18.25	19.20	ISLL
2004	7	15	18.00	19.50	18.25	19.20	GILL
2004	7	15	18.00	19.50	18.25	19.20	CHUR
2004	7	15	18.00	19.50	18.25	19.20	RANK
2004	7	15	18.00	19.50	18.25	19.20	RABB
2004	7	15	18.00	19.50	18.25	19.20	FSMI
2004	7	15	18.00	19.50	18.25	19.20	MCMU
2004	7	15	18.00	19.50	18.25	19.20	DAWS
2004	8	17	17.00	23.83	18.00	23.00	PINA
2003	11	4	19.00	21.00	19.50	20.68	ISLL
2003	11	4	19.00	21.00	19.50	20.90	GILL
2003	11	4	19.00	21.00	19.50	20.90	CHUR
2003	11	4	19.00	21.00	19.50	20.90	RABB
2003	11	4	19.00	21.00	19.50	20.90	FSMI
2003	11	4	19.00	21.00	19.50	20.70	DAWS
2003	3	17	18.50	20.00	19.11	19.31	GILL
2003	3	17	18.50	20.00	19.10	19.31	ESKI
2003	3	17	18.50	20.00	19.10	19.60	RANK
2003	3	17	18.50	20.00	19.10	19.31	MCMU
2003	3	17	18.50	20.00	19.10	19.31	CONT
2002	7	20	20.00	23.00	21.75	22.90	PINA
2002	7	20	20.00	23.00	21.75	22.90	MCMU
2002	7	20	20.00	23.00	21.75	22.90	CONT
2002	7	20	20.00	23.00	21.75	22.80	DAWS

Flare YYYY	Month MM	Day DD	Start Decimal Hours	End Decimal Hours	Fit Start	Fit End	Station ID
2001	4	2	21.00	23.00	21.50	21.85	CHUR
2001	4	2	21.00	23.00	21.50	21.85	ESKI
2001	4	2	21.00	23.00	21.50	21.85	RANK
2001	4	2	21.00	23.00	21.50	22.85	TALO
2001	8	25	15.00	23.00	16.90	18.50	PINA
2001	8	25	16.00	18.83	16.90	18.25	CHUR
2001	8	25	16.00	18.83	16.90	18.25	RANK
2001	8	25	16.00	18.83	16.90	18.25	RABB
2001	8	25	16.00	18.83	16.90	18.25	FSMI
2001	8	25	16.00	18.83	16.90	18.25	MCMU
2001	9	17	15.00	23.00	15.60	17.00	PINA
2000	6	7	15.00	17.00	15.51	16.00	PINA
2000	6	7	15.00	17.00	15.50	16.00	ISLL
2000	6	7	15.00	17.00	15.50	16.00	GILL

## APPENDIX B. CONTROL FLARE LIST

Appendix B contains all the flare events of the control list, used as a control group to test the efficacy of our model's performance. It is comprised more of M class flares than the model list. Similar to Appendix A, the flares are listed by date. The fitting window and flare start time are in decimal hours with the riometer station code included.

Flare	Month	Day	Start Decimal	End Decimal	Fit Start	Fit End	Station ID
YYYY	MM	DD	Hours	Hours			
2005	8	2	15.00	23.00	18.69	19.00	PINA
2005	8	2	15.00	23.00	18.50	19.00	GILL
2005	8	2	15.00	23.00	18.20	19.00	ESKI
2005	8	2	15.00	23.00	18.20	19.00	TALO
2005	8	2	15.00	23.00	18.20	19.00	RANK
2005	8	2	15.00	23.00	18.20	19.00	ISLL
2005	8	2	15.00	23.00	18.20	19.00	DAWS
2005	8	2	15.00	23.00	18.20	19.00	CHUR
2005	8	2	15.00	23.00	18.20	19.00	CONT
2005	8	2	15.00	23.00	18.20	19.00	MCMU
2005	8	2	15.00	23.00	18.20	19.00	FSMI
2004	8	17	15.00	23.00	19.40	20.50	PINA
2004	8	17	15.00	23.00	19.40	20.50	GILL
2004	8	17	15.00	23.00	19.40	20.50	RANK
2004	8	17	15.00	23.00	19.40	20.50	TALO
2004	8	17	15.00	23.00	19.40	20.50	RABB
2004	8	17	15.00	23.00	19.40	20.50	CHUR
2004	8	17	15.00	23.00	19.40	20.50	CONT
2004	8	17	15.00	23.00	19.40	20.50	ISLL
2004	8	13	18.00	19.50	18.10	18.40	PINA
2004	8	13	18.00	19.50	18.10	18.40	GILL
2004	8	13	18.00	19.50	18.10	18.40	ESKI
2004	8	13	18.00	19.50	18.10	18.40	TALO
2004	8	13	18.00	19.50	18.10	18.40	RANK
2004	8	13	18.00	19.50	18.10	18.40	RABB
2004	8	13	18.00	19.50	18.10	18.40	CHUR
2004	8	13	18.00	19.50	18.10	18.40	CONT
2004	8	13	18.00	19.50	18.10	18.40	ISLL
2004	8	13	18.00	19.50	18.10	18.40	FSMI
2004	8	13	18.00	19.50	18.10	18.40	MCMU
2004	7	13	18.00	23.50	18.37	19.90	PINA
2004	7	13	18.00	23.50	18.37	19.90	GILL

Flare	Month	Day	Start Decimal	End Decimal	Fit	Fit	Station
YYYY	MM	DD	Hours	Hours	Start	End	ID
2004	7	13	18.00	23.50	18.37	19.90	ESKI
2004	7	13	18.00	23.50	18.37	19.90	TALO
2004	7	13	18.00	23.50	18.37	19.90	RANK
2004	7	13	18.00	23.50	18.37	19.90	RABB
2004	7	13	18.00	23.50	18.37	19.90	CONT
2004	7	13	18.00	23.50	18.37	19.90	DAWS
2004	7	13	18.00	23.50	18.37	19.90	MCMU
2003	3	17	18.50	20.00	18.80	19.50	GILL
2003	3	17	18.50	20.00	18.80	19.50	ESKI
2003	3	17	18.50	20.00	18.80	19.50	TALO
2003	3	17	18.50	20.00	18.80	19.50	RANK
2003	3	17	18.50	20.00	18.80	19.50	RABB
2003	3	17	18.50	20.00	18.80	19.50	CHUR
2003	3	17	18.50	20.00	19.80	19.50	FSMI
2003	3	17	18.50	20.00	19.80	19.50	ISLL
2001	8	25	15.00	23.00	16.83	18.40	PINA
2001	8	25	15.00	23.00	16.83	18.40	ESKI
2001	8	25	15.00	23.00	16.83	18.40	RANK
2001	8	25	15.00	23.00	16.83	18.40	RABB
2001	8	25	15.00	23.00	16.83	18.40	CHUR
2001	8	25	15.00	23.00	16.83	18.40	CONT
2001	8	25	15.00	23.00	16.83	18.40	DAWS
2001	8	25	15.00	23.00	16.83	18.40	MCMU
2001	8	25	15.00	23.00	16.83	18.40	FSMI
2001	8	25	15.00	23.00	16.83	18.40	ISLL
2000	6	7	15.00	17.00	15.50	16.15	RABB
2000	6	7	15.00	17.00	15.50	16.15	CHUR
2000	6	7	15.00	17.00	15.50	16.15	CONT
2000	6	7	15.00	17.00	15.50	16.15	MCMU
2000	6	7	15.00	17.00	15.50	16.15	ISLL

## LIST OF REFERENCES

- Akmaev, R. A. (2010). *D-RAP Model Validation: I. Scientific Report*. National Oceanic and Atmospheric Administration. <https://www.ngdc.noaa.gov/stp/drap/DRAP-V-Report1.pdf>
- Brodrick, D., Tingay, S., & Wieringa, M. (2005). X-ray magnitude of the 4 November 2003 solar flare inferred from the ionospheric attenuation of the galactic radio background. *Journal of Geophysical Research: Space Physics*, *110*(A9). <https://doi.org/10.1029/2004JA010960>
- Cliver, E. W., & Dietrich, W. F. (2013). The 1859 space weather event revisited: Limits of extreme activity. *Journal of Space Weather and Space Climate*, *3*(A31). <https://doi.org/10.1051/swsc/2013053>
- Contreira, D. B., Rodrigues, F. S., Makita, K., Brum, C. G. M., Gonzalez, W., Trivedi, N. B., et al. (2005). An experiment to study solar flare effects on radio-communication signals. *Advances in Space Research*, *36*(12), 2455–2459. <https://doi.org/10.1016/j.asr.2004.03.019>
- Davies, K. (1990). *Ionospheric radio*. Peter Peregrinus Ltd., London. <http://dx.doi.org/10.1049/PBEW031E>
- Eccles, J. V., Hunsucker, R. D., Rice, D., & Sojka, J. J. (2005). Space weather effects on midlatitude HF propagation paths: Observations and a data-driven D region model: Data-driven D region model. *Space Weather*, *3*(1). <https://doi.org/10.1029/2004SW000094>
- European Space Agency. (2021, April 14). *Solar Particle Event Archive*. [Data set] ESA Space Environment. <https://space-env.esa.int/noaa-solar-proton-event-archive/>
- Harvey, G. A. (1965). 2800 Megacycle per second radiation associated with type II and type IV solar radio bursts and the relation with other phenomena, *J. Geophys. Res.*, *70*(13). 2961-2976. <https://doi.org/10.1029/JZ070i013p02961>
- Hargreaves J. K. (1969). Auroral absorption of HF radio waves in the ionosphere: A review of results from the first decade of riometry. *Proceedings of the IEEE*. *57*(8) 1348-1373. doi:10.1109/proc.1969.7275.
- Hultqvist, B. (1966) Ionospheric absorption of cosmic radio noise. *Space Sci Rev.* *5*, 771-817. <https://doi.org/10.1007/BF00173104>

- Kiplinger, A.L., Garcia, H.A. (2004). Soft x-ray parameters of the great flares of active region 486, *Bull. Am. Astron. Soc.*, 36, 739.  
[https://www.researchgate.net/publication/260071270\\_Soft\\_X-ray\\_Parameters\\_of\\_the\\_Great\\_Flares\\_of\\_Active\\_Region\\_486](https://www.researchgate.net/publication/260071270_Soft_X-ray_Parameters_of_the_Great_Flares_of_Active_Region_486)
- Kutiev, I. (2010). *The Earth's Plasmasphere and Topside Ionosphere*. Geophysical Institute, BAS, Sofia, Bulgaria.  
[Indico.ictp.it/event/a09174/session/33/contribution/22/material/0/0.pdf](http://Indico.ictp.it/event/a09174/session/33/contribution/22/material/0/0.pdf)
- Longden, N., Denton, M. H., and Honary, F. (2008), Particle precipitation during ICME-driven and CIR-driven geomagnetic storms, *J. Geophys. Res.*, 113(A6) 205, doi:10.1029/2007JA012752.
- Matzka J., Stolle C., Yamazaki Y., Bronkalla A., Morschhauser A., (2021). The geomagnetic Kp index and derived indices of geomagnetic activity. *Space Weather* 19(5). <https://doi.org/10.1029/2020SW002641>
- Marshall, R. A. & Cully, C. M. (2020), Atmospheric effects and signatures of high-energy electron precipitation. In A. Janes and M.E Usanova (Eds.), *The dynamic loss of Earth's radiation belts*. (1st ed., pp. 199-255). Elsevier.  
<https://doi.org/10.1016/B978-0-12-813371-2.00007-X>
- Möller A. (2021). *Aurora Forecast for Germany* [Data set]. Space Weather Prediction Center. <https://www.polarlicht-vorhersage.de/goes-archive>
- National Aeronautics and Space Administration. (2011, August 9). *What does it take to be X-class?* [https://www.nasa.gov/mission\\_pages/sunearth/news/X-class-flares.html](https://www.nasa.gov/mission_pages/sunearth/news/X-class-flares.html)
- National Aeronautics and Space Administration. (2013, January 22). *Earth's Atmospheric Layers*. [https://www.nasa.gov/mission\\_pages/sunearth/science/atmosphere-layers2.html](https://www.nasa.gov/mission_pages/sunearth/science/atmosphere-layers2.html)
- National Atmospheric and Science Administration. (2015, March 6). *What is a Solar Prominence?* NASA. <https://www.nasa.gov/content/goddard/what-is-a-solar-prominence>
- National Atmospheric and Science Administration. (2020, May 22). *What is a Geomagnetic Storm?* NASA.  
[https://www.nasa.gov/mission\\_pages/sunearth/spaceweather/index.html#q7](https://www.nasa.gov/mission_pages/sunearth/spaceweather/index.html#q7)
- National Center for Atmospheric Research. (2009). *Magnetic Field Lines Tangle as Sun Rotates*. UCAR. <https://scied.ucar.edu/video/sun-magnetic-field-rotate-tangle-movie#:~:text=Over%20time%2C%20the%20Sun's%20differential,active%20regions%20where%20sunspots%20form.>

- National Oceanic and Atmospheric Administration. (2004, April). *X28 extrapolation Service Assessment Intense Space Weather Storms October 19 – November 07, 2003.pdf*.  
[https://www.weather.gov/media/publications/assessments/SWstorms\\_assessment.pdf](https://www.weather.gov/media/publications/assessments/SWstorms_assessment.pdf)
- National Oceanic and Atmospheric Administration. (2012a). *Solar Radio Bursts Fixed Frequency* [data set]. NOAA. <https://www.ngdc.noaa.gov/stp/space-weather/solar-data/solar-features/solar-radio/radio-bursts/reports/fixed-frequency-listings/>
- National Oceanic and Atmospheric Administration (2012b). *Readme: Solar radio bursts*.  
[https://www.ngdc.noaa.gov/stp/space-weather/solar-data/solar-features/solar-radio/radio-bursts/reports/fixed-frequency-listings/documentation/dataset-description\\_solar-radio\\_bursts\\_fixed-frequency\\_listings.pdf](https://www.ngdc.noaa.gov/stp/space-weather/solar-data/solar-features/solar-radio/radio-bursts/reports/fixed-frequency-listings/documentation/dataset-description_solar-radio_bursts_fixed-frequency_listings.pdf)
- National Oceanic and Atmospheric Administration. (2020). *GOES XRS X-ray data* [Unpublished raw data]. <https://ngdc.noaa.gov/stp/satellite/goes/dataaccess.html>
- National Oceanic and Atmospheric Administration. (2021a, April). *Geomagnetic Kp and Ap indices*. NOAA. [https://www.ngdc.noaa.gov/geomag/indices/kp\\_ap.html](https://www.ngdc.noaa.gov/geomag/indices/kp_ap.html)
- National Oceanic and Atmospheric Administration. (2021b). *Solar Proton Events Affecting the Earth Environment*. [Data set] Space Environment Services Center.  
<https://umbra.nascom.nasa.gov/SEP/>
- Ogunmodimu, O., Honary, F., Rogers, N., Falayi, E. O., & Bolaji, O. S. (2018). Solar flare induced cosmic noise absorption. *NRIAG Journal of Astronomy and Geophysics*, 7(1), 31–39. <https://doi.org/10.1016/j.nrjag.2018.03.002>
- Olsen, R. C. (2005). *Introduction to the space environment*. [course text]. Naval Postgraduate School.
- Patterson, J. D., Armstrong T. P, Laird C. M., Detrick D. L., Weatherwax, A. T. (2002) Correlation of solar energetic protons and polar cap absorption. *J. Geophys. Res.*, 107(A12), <https://doi.org/10.1029/2000JA002006>
- Poole, I. (n.d.). *Lowest and Maximum usable frequency, critical frequency*. Electronics Notes. Retrieved July 7, 2021, from <https://www.electronics-notes.com/articles/antennas-propagation/ionospheric/maximum-lowest-critical-optimum-usable-working-frequency.php>
- Redmon, R. J., Seaton, D. B., Steenburgh, R., He, J., & Rodriguez, J. V. (2018). September 2017's Geoeffective space weather and impacts to Caribbean radio communications during hurricane response. *Space Weather*, 16(9), 1190–1201. <https://doi.org/10.1029/2018SW001897>

- Rogers, N. C., & Honary, F., Hallam, J. Stocker, A. J., Warrington, E. M., Siddle, D. R., Danskin, D. W., Jones, B. (2015a). Assimilative real-time models of HF absorption at high latitudes, *In Proceedings of the 14th International Ionospheric Effects Symposium*. (pp. 1-8). [48]. <http://ies2015.bc.edu>
- Rogers, N. C., & Honary, F. (2015b). Assimilation of real-time riometer measurements into models of 30 MHz polar cap absorption. *Journal of Space Weather and Space Climate*, 5(A8). <https://doi.org/10.1051/swsc/2015009>
- Rogers, N. C., Kero, A., Honary, F., Verronen, P. T., Warrington, E. M., & Danskin, D. W. (2016). Improving the twilight model for polar cap absorption nowcasts: Twilight model for PCA nowcasts. *Space Weather*, 14(11), 950–972. <https://doi.org/10.1002/2016SW001527>
- Rose, D. C., Ziauddin, S. (1962). The polar cap absorption effect. *Space Science Reviews*, 1(1), 115-134. <https://doi.org/10.1007/BF00174638>
- Sauer, H. H., & Wilkinson, D. C. (2008). Global mapping of ionospheric HF/VHF radio wave absorption due to solar energetic protons: Ionospheric radiowave absorption. *Space Weather*, 6(S12), 002. <https://doi.org/10.1029/2008SW000399>
- Schumer, E. A. (2010). Improved modeling of midlatitude D-Region ionospheric absorption of high frequency radio signals during solar x-ray flares, (Doctoral dissertation). Retrieved from AFIT Scholar (<https://scholar.afit.edu/etd/2155/>). Wright-Patterson Air Force Base, OH: Air Force Institute of Technology.
- Space Weather Live. (2021, May 11). *The Kp-index*. <https://www.spaceweatherlive.com/en/help/the-kp-index.html>
- Space Weather Prediction Center. (2010, May 11). *Global D-region absorption prediction documentation*. <https://www.swpc.noaa.gov/content/global-d-region-absorption-prediction-documentation>
- Space Weather Prediction Center. (2019, Oct 8). *Why space radiation matters*. <https://www.nasa.gov/analog/nsrl/why-space-radiation-matters>
- Space Weather Prediction Center. (2021a, April 8). *NOAA scales explanation*. <https://www.swpc.noaa.gov/noaa-scales-explanation>
- Space Weather Prediction Center. (2021b, April 8). *Solar Flare Radio Blackouts*. <https://www.swpc.noaa.gov/phenomena/solar-flares-radio-blackouts#:~:text=Solar%20flares%20are%20large%20eruptions,lasting%20from%20minutes%20to%20hours.&text=This%20results%20in%20a%20radio,3%20to%2030%20MHz%20band.>

- Space Weather Prediction Center. (2021c, April 12). *D-Region absorption predictions (D-RAP)* <http://www.swpc.noaa.gov/products/d-region-absorption-predictions-d-rap>
- Space Weather Prediction Center. (2021d, July 25). *Planetary K-index*. <https://www.swpc.noaa.gov/products/planetary-k-index>
- Stonehocker G. H. (1970) Advanced telecommunication forecasting technique. Advisory Group for Aerospace Research & Development Conference 49, (27-27-5). <https://apps.dtic.mil/dtic/tr/fulltext/u2/700896.pdf>
- Theusner M. (2021) *Kp-Index and Kpa-Index archive*. [Data set]. [http://www.theusner.eu/terra/aurora/kp\\_archive.php](http://www.theusner.eu/terra/aurora/kp_archive.php)
- Thomson, N. R., Rodger, C. J., & Dowden, R. L. (2004). Ionosphere gives size of greatest solar flare: Size of the greatest solar flare. *Geophysical Research Letters*, 31(6). <https://doi.org/10.1029/2003GL019345>
- Tranquille, C., Hurley, K., Hudson, H.S, (2009). The Ulysses catalog of solar hard x-ray flares, *Solar Phys.*, 258, 141-166. <https://doi.org/10.1007/s11207-009-9387-9>
- Tsiftsi, T., & De la Luz, V. (2018). Extreme value analysis of solar flare events. *Space Weather*, 16(12), 1984–1996. <https://doi.org/10.1029/2018SW001958>
- University of Calgary. (2005). *Canopus Riometer Baselineing Technique*. [https://aurora.phys.ucalgary.ca/norstar/rio/doc/CANOPUS\\_Riometer\\_Baselineing.pdf](https://aurora.phys.ucalgary.ca/norstar/rio/doc/CANOPUS_Riometer_Baselineing.pdf)
- University of Calgary. (2021). Riometer [Data Set]. University of Calgary Space Physics Group. [https://data.phys.ucalgary.ca/sort\\_by\\_project/GO-Canada/GO-Rio/IDLsav/](https://data.phys.ucalgary.ca/sort_by_project/GO-Canada/GO-Rio/IDLsav/)
- Warrington, E. M., Zaalov, N. Y., Naylor, J. S., & Stocker, A. J. (2012). HF propagation modeling within the polar ionosphere: Polar HF propagation modeling. *Radio Science*, 47(4). <https://doi.org/10.1029/2011RS004909>
- Warrington, E. M., Stocker, A. J., Siddle, D. R., Hallam, J., Al-Behadili, H. A. H., Zaalov, N. Y., et al. (2016). Near real-time input to a propagation model for nowcasting of HF communications with aircraft on polar routes: HF communications for polar routes. *Radio Science*, 51(7), 1048–1059. <https://doi.org/10.1002/2015RS005880>
- Watanabe, K., Masuda S., Segawa T. (2012). Hinode Flare Catalogue [Data set]. *Solar Physics* 279, 317-322. Retrieved from [https://xrt.cfa.harvard.edu/flare\\_catalog/](https://xrt.cfa.harvard.edu/flare_catalog/)

- Woods, T. N., Eparvier, F. G., Fontenla, J., Harder, J., Kopp, G., McClintock, W. E. (2004). Solar irradiance variability during the October 2003 solar storm period. *Geophysical Research Letters*, *31*(10). <https://doi.org/10.1029/2004GL019571>
- White House. (2015). [https://obamawhitehouse.archives.gov/sites/default/files/microsites/ostp/final\\_national\\_space\\_weather\\_action\\_plan\\_20151028.pdf](https://obamawhitehouse.archives.gov/sites/default/files/microsites/ostp/final_national_space_weather_action_plan_20151028.pdf)
- Yasyukevich, Y., Astafyeva, E., Padokhin, A., Ivanova, V., Syrovatskii, S., & Podlesnyi, A. (2018). The 6 September 2017 x-class solar flares and their impacts on the ionosphere, GNSS, and HF Radio Wave Propagation. *Space Weather*, *16*(8), 1013–1027. <https://doi.org/10.1029/2018SW001932>
- Zhong, J., Lei, J., Wang, W., Burns, A., Yue, X., Dou, X. (2017). Longitudinal variations of topside ionospheric and plasmaspheric TEC. *JGR Space Physics*, *122*(6). <https://doi.org/10.1002/2017JA024191>

## INITIAL DISTRIBUTION LIST

1. Defense Technical Information Center  
Ft. Belvoir, Virginia
2. Dudley Knox Library  
Naval Postgraduate School  
Monterey, California